Department of AERONAUTICS and ASTRONAUTICS
STANFORD UNIVERSITY

KENNETH P. HORN

RADIATIVE BEHAVIOR OF SHOCK HEATED ARGON PLASMA FLOWS

SUBMITTED BY D. BERSHADER

MAY 1966

Jointly supported by the National Aeronautics and Space Administration, Grant NGR 05-020-091 and by a Ford Foundation Plasma Grant

SUDAAR NO. 268*

*also issued as SU-IPR Report No. 79 of the Institute for Plasma Research, Stanford University

Department of Aeronautics and Astronautics
Stanford University
Stanford, California

RADIATIVE BEHAVIOR OF SHOCK GENERATED ARGON PLASMA FLOWS

by

Kenneth P. Horn

SUDAAR 268

May 1966

Submitted by D. Bershader

Jointly supported by the
National Aeronautics and Space Administration,
Grant NGR 05-020-091 and by a
Ford Foundation Plasma Grant

This Report was also Issued as Report No. 79 of
the Institute for Plasma Research, Stanford University

30609

ABSTRACT

Experimental and theoretical studies were made of the decrease in the degree of ionization of shock heated argon resulting from radiative emission. Optical interferometry used in conjunction with a rotating mirror camera provided a time history of the mass and electron densities following strong shocks. After a short electronic relaxation period the hot, highly luminous gas reached local thermodynamic equilibrium. Then, loss of energy by radiation led to cooling of the gas as evidenced by the decreasing electron density. On the assumption that the dense plasma (10^{17} electrons per cc) passed through successive equilibrium states upon cooling, the change in the temperature and in the number density of the electrons could be related by use of the Saha equation. The change in degree of ionization thus determined was compared with calculated values, assuming continuum emission by free-free and free-bound transitions and emission from spectral lines. Theory and experiment were in good agreement, for a realistic choice of the parameters contained in the continuum theory. The analysis indicated that line radiation losses could not be disregarded. Sizable loss resulted from lower lever bound-bound transitions even though these lines experienced absorption. Various radiation absorption models were investigated.

ACKNOWLEDGMENTS

The author would like to express his sincere appreciation to Dr. Daniel Bershader for his very enlightening discussions and supervision during the various stages of the thesis research. Also the author gratefully acknowledges the assistance of the following persons: Peter Oettinger for stimulating conversations and constant interest, David Barnett for his mathematical assistance, Dr. H. Wong for his help and advice, Roger Turcotte for his excellent design and construction of the experimental apparatus, and Rosemarie Stampfel for her typing.

The research program was supported by the Advanced Research Projects Agency, the Ford Foundation, and the National Aeronautics and Space Administration.

TABLE OF CONTENTS

LIST OF TABLES AND FIGURES

LIST OF TABLES AND FIGURES Cont.

LIST OF SYMBOLS

A	argon; Einstein A coefficient
a	polarizability
A^*	$\frac{e^2 Nf}{m_e c}\ (1 - e^{-h\nu_o/kT})$
a_e	equilibrium speed of sound
B	$\Gamma/4\pi$
B_ν	Planck distribution
c	speed of light
C_4	quadratic Stark constant
e	electronic charge; internal energy
E	energy
E_{ex}	excitation temperature
f	distribution function; oscillator strength
g	degeneracy
h	enthalpy; Planck's constant
I_ν	specific intensity
j_ν	mass emission coefficient
K_ν	mass absorption coefficient
k_ν	volume absorption coefficient
k	Boltzmann coefficient
L	length
ℓ	azimuthal quantum number

M	Mach number; atomic weight
m_a	argon mass
m_e	electron mass
N	number density
N_a	atom number density
N_e	electron number density
n	principal quantum number; index of refraction
p	pressure
Q	energy loss per unit volume per unit time
R	gas constant; radius of shock tube; radial distance
R_y	Rydberg constant
r	radial distance
S	line strength
T	temperature
T_e	electron temperature
t	time
u	velocity
V	potential
v	particle velocity
x	distance
Z	nuclear charge
Z_{eff}	effective nuclear charge parameter
z_A^{el}	atom electronic partition function
z_i^{el}	ion electronic partition function

α degree of ionization $\frac{N_e}{N_e + N_A}$

α_{BF} bound-free atomic absorption coefficient

α_{FF} free-free atomic absorption coefficient

β angle; $\frac{hR_y}{kT}$

Γ half width

γ multiplicity factor

γ^* isentropic index

δ fringe shift

ϵ energy eigenvalue; emission per unit frequency

$\zeta(\nu)$ zeta function

θ ionization temperature; angle

λ wavelength

σ^2 transition integral

ν frequency

μ deflection angle; reduced mass

ρ density

θ_{pn} photoionization cross section

τ_ν optical depth

Ω solid angle

ω angular frequency

ω_p plasma frequency

1. INTRODUCTION

This study is part of an extended series of investigations being performed at Stanford University, which deal with the recombination and radiation phenomena associated with thermal ionization of argon gas. The ionization is induced by strong normal shock waves generated in a conventional combustion driven shock tube. The experimental technique employed to study the effect of recombination and radiation phenomena utilizes a Mach-Zehnder interferometer, which monitors with time both the electron density and the heavy particle density. This study was undertaken in order to obtain information on the effect of radiative behavior of shock heated argon plasma flows.

As a strong shock propagates into quiescent argon, the gas undergoes an extremely rapid increase in enthalpy. The statistical equilibrium is temporarily destroyed, and a finite relaxation period exists before the gas species reach thermodynamic equilibrium. An interferometric study of the thermal equilibration of shock heat argon by Wong (1) showed that the gas reaches thermodynamic equilibrium as predicted by the Saha equation. This occurs after a short nonequilibrium electronic relaxation zone. In the latter part of this equilibration process visible radiation becomes apparent. As a consequence of this radiation loss, the enthalpy of the gas is appreciably reduced, and the transient Saha equilibrium state is altered.

The first part of this research study deals with the radiation losses, including both line and continuum emission, associated with the flow behind the incident shock wave outside the relaxation zone. By monitoring the electron density the effect of the energy loss can be observed, and degree of ionization profiles can be experimentally determined. Knowing the atomic constants for the various radiative transitions, the total energy loss resulting from radiative emission can be calculated. Thus comparison can be made between the experimental results and the theoretical predictions.

The subject of radiation "cooling" has been considered by several investigators in the last few years. Radiation cooling seems to really be a misnomer since the gas temperature is a slowly varying function of time.

Petschek et al. (2) first considered the radiative losses associated with highly ionized argon. They assumed that the Kramers-Unsöld formula for continuous emission described the radiation energy loss. Spectrophotometry results showed good agreement with theoretical results, using however an arbitrary set of values for unknown parameters contained in the continuum theory.

Pomerantz (3) improved the calculations by removing certain low degree of ionization approximations and by including the effect of lowering of the ionization potential. However he likewise assumed only continuum radiative losses. He did investigate the influence of absorption for high gas pressures, unfortunately for the case of a plane infinite shock.

Recently McChesney and Al-Attar (4) reconsidered the problem of continuum radiation from shock heated argon. Their results are essentially the same as Pomerantz's case of no absorption, except for the use of Debye polarization theory to account for lowering of the ionization potential.

Sevastyaneko and Yakubov (5) first investigated theoretically the heretofore neglected effect of line radiation. Their results indicate that line radiation losses can be sizable. However, no side experiments were conducted and their results could only be compared with the old Petschek et al. spectrophotometry data.

Dronov et al. (6) studied experimentally the brightness and energy distribution of krypton and xenon. However they assumed only continuum emission and hence compared their results with the Kramers-Unsöld theory.

Alpher and White (7) measured relative intensities in the visible continuum emitted by shock-ionized argon, krypton, and xenon. The data seemed to correlate well with the Kramers-Unsöld theory, thus indicating that free-bound electron transitions were the primary source of the continuum radiation.

Rutowski and Bershader (8) measured radiative heat transfer in the stagnation region of a blunt body in a high electron density argon flow. Again they found the Kramers-Unsöld continuum radiation loss explained their experimental results under a suitable choice of the parameter inherent in the continuum theory.

One must note that the Kramers-Unsöld theory strictly applies only for hydrogenic atoms. Recent theoretical studies (9, 10) indicate that this theory describes rather poorly the actual emission for the complex noble gases.

Therefore it was felt that a thorough reexamination of the mechanisms of radiation losses was required along with experimental results determined from a new diagnostic technique. By application of a Mach-Zehnder interferometer in conjunction with a rotating mirror camera, electron density profiles in the radiating flow region could be recorded. To compliment this technique, photometry and spectroscopy were incorporated at times to monitor the flow. These measurements gave an insight into the atomic phenomena of radiation.

A second phase of this work dealt with an application of the results of the first study. It was desired to produce as near as possible a uniform sample of plasma in order that a steady state, ionized, Prandtl-Meyer expansion could be experimentally investigated. Such a resulting expansion flow hopefully would give additional insight into the associated recombination phenomena. Unfortunately adequate fringe shift could only be obtained under severe nonsteady flow conditions. Interpretation of the experimental data was difficult under such a nonsteady flow situation. This subject is discussed in detail in Appendix 4.

The visible light emitted from a hot, highly ionized, shock heated gas is due to emission from numerous radiative processes.

A rather laborious discussion is required before one can hope to understand fully these various emission mechanisms. Therefore the next section examines the atomic structure of a radiating argon plasma and expressions for the emission resulting from first line radiation and then continuum radiation are derived. For optically thin continuum radiation such an approach is usually unnecessary, however since absorption of certain spectral lines is experienced under the test conditions, for the present study such an approach is essential. Also in this chapter the governing flow equations are introduced.

Next, the experimental method and apparatus are discussed in Chapter 3, while in Chapter 4 comparison is made between the experimental data and the theoretical predictions. Conclusions and additional comments are presented in the last section.

2. RADIATION LOSSES

The radiation losses resulting in visible luminosity from shock heated argon gas are essentially due to three emission processes which occur simultaneously. These processes are:

1. Free-free transitions, or Bremsstrahlung radiation

   $A^+ + e \rightarrow A^+ + e + h\nu$

   $A + e \rightarrow A + e + h\nu$

2. Free-bound transitions, which involve radiative recombination resulting in quantization of the final energy

   $A^+ + e \rightarrow A(p) + h\nu$

3. Bound-bound atomic transitions

   $A(p) \rightarrow A(q) + h\nu_{pq}$ (spontaneous emission)

   $A(p) + h\nu \rightarrow A(q) + h\nu + h\nu_{pq}$ (stimulated emission)

The first two processes result in continuum radiation since they involve free electrons, while the third process results in line radiation since both states are quantized.

Several possible approaches are available to estimate the total emitted radiation loss, but all basically require a knowledge of the number of emitter, the energy released through the process, and the transition probabilities which express the chance that such a transition occurs. The approach chosen for the present study stresses the importance of absorption of energy, in which an understanding of the geometry of the luminous region is required.

This influence of absorption of energy presents the usual mathematical difficulty in solving radiation gasdynamics problems.

2.1 General Radiation Theory

The theory of radiative transfer is based on the conservation of radiant energy. Consider a medium in which there is both emission as well as absorption. The conservation equation relates the rate of change in the specific intensity to the emission in the element minus the energy absorbed. Mathematically the transfer equation has the following form, (11)

$$\frac{1}{c}\frac{\partial I_\nu}{\partial t} + \ell_j \frac{\partial I_\nu}{\partial x_j} = \rho(j_\nu - I_\nu K'_\nu)$$

where I_ν is the specific intensity along a certain direction in which the quanta $h\nu$ are propagated, j_ν is the mass emission coefficient, K'_ν is the mass absorption coefficient which includes induced emission, and ℓ_j are the direction cosines of the direction of propagation with respect to the positive coordinate axis.

If the time derivative term is neglected then a formal solution for the transfer of radiation can be obtained. Near thermal equilibrium Kirchhoff's law can be used to relate the emission coefficient to the absorption coefficient using the Planck blackbody distribution function, B_ν. Under such quasi-equilibrium conditions the form for the radiative transfer equation becomes,

$$\ell_j \frac{\partial I_\nu}{\partial x_j} = k'_\nu (B_\nu - I_\nu)$$

in which the mass absorption coefficient is related to the volume absorption coefficient k'_ν by,

$$k'_\nu = K'_\nu \rho = k_\nu (1 - e^{-h\nu/kT})$$

where in the latter form the factor $(1 - e^{-h\nu/kT})$ is the correction to k_ν that results from induced emission. The absorption coefficient must include the effects of bound-bound, bound-free, and free-free transitions.

The solution for the specific intensity at $r = 0$ with a boundary value of $I_\nu(R)$ at $r = R$ is, (11)

$$I_\nu(r = 0) = I_\nu(R)\, e^{-\int_0^R k'_\nu dr} + \int_0^R B_\nu\, k'_\nu\, e^{-\int_0^r k'_\nu\, d\tilde{r}}\, dr$$

where r is measured from the point in question in the direction opposite to the direction of propagation of the radiation. The dimensionless optical depth at frequency ν can then be defined by,

$$\tau_\nu(r) = \int_0^r k'_\nu\, d\tilde{r} \,.$$

The question then arises--how do the radiation effects alter the equations of motion of a radiating gas? The continuity equation is obviously unchanged. However since the radiation

flux transfers momentum and energy, the momentum and energy equations must be altered. For such a shock tube experiment the radiation pressure is negligibly small compared to the gas pressure. Therefore only the energy equation accounts for the radiation phenomena. Since a particle both emits and absorbs energy, the energy equation takes the following form, (12)

$$\rho \frac{d}{dt} (e + u^2/2) + \text{div } p \vec{u} = - 4\pi \int_\nu k'_\nu B_\nu d\nu + \int_\nu \int_\Omega k'_\nu I_\nu d\Omega \, d\nu$$

where the first term on the right hand side expresses the rate of energy emitted by a volume element and the second term the rate of energy absorbed by that element. Notice that the first term is isotropic (a function of ν and r), while the second term is a function of direction. This nonisotropic character of I_ν presents the mathematical difficulty in solving a shock tube flow problem. Pomerantz (3) has solved the absorption problem for a stratified medium with a cross section which is infinite in extent. This over simplified problem does not represent the actual shock tube geometry. Other mathematically simplified models can be chosen which approximate the actual problem without introducing difficult computations.

At this time it is necessary to anticipate slow cooling rates. Since the portions of the luminous gas influence absorption only in the region near the point in question, it then seems reasonable to assume as a first approximation that the luminous

gas is all at the same local equilibrium temperature and density, determined at that point. Thus B_ν and k'_ν are functions of time. For strong shocks the electronic relaxation zone is very short and its effect on absorption will be neglected. Therefore the sample of highly luminous gas is bounded between the "ionization" front and the "cold" front. If one then assumes a finite gas volume within this sample of radiative gas with uniform temperature and density, both B_ν and k'_ν are constants in the region for any given time. The sketch below illustrates schematically this flow geometry.

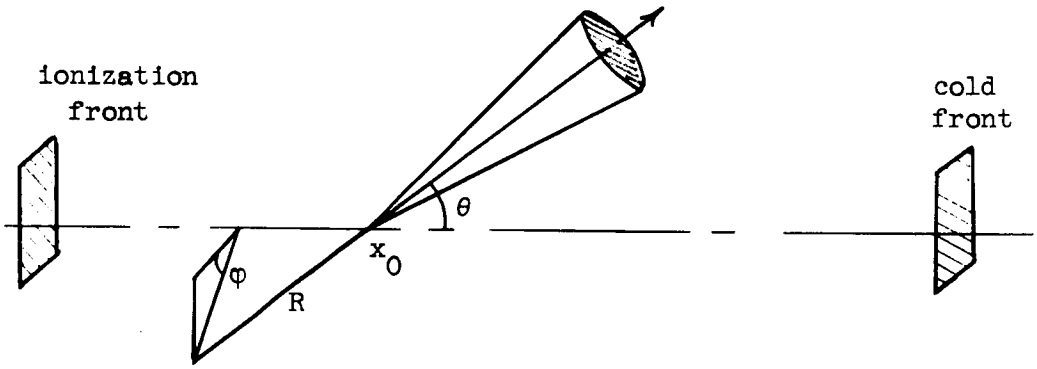

If also the boundary value at $r = R$ is assumed zero, the specific intensity at $r = 0$ reduces simply to,

$$I_\nu = B_\nu(1 - e^{-k'_\nu R})$$

where the dependence on direction angle is limited to the expression for R. For $k'_\nu R \gg 1$ the gas sample is optically thick and $I_\nu \to B_\nu$, while for $k'_\nu R \ll 1$ the gas sample is thin and $I_\nu \to k'_\nu B_\nu R$.

For the case of axial symmetry the right hand side of the energy equation then becomes,

$$-2\pi \int_{\nu} \int_{\theta} k'_{\nu} B_{\nu} e^{-k'_{\nu} R} \sin\theta \, d\theta \, d\nu = - Q$$

where the shape of the assumed absorption domain is described by $R = R(\theta)$. The symbol Q represents the total energy loss per unit volume per unit time. As expected for the optically thin case $(\tau_{\nu} \to 0)$ the expression for Q reduces to $4\pi \int_{\nu} k'_{\nu} B_{\nu} d\nu$. This is simply the expression for the rate of energy emitted, since there is no absorption. This expression can be used for the continuum radiation loss, as it will be presently shown that such radiation under the test conditions is indeed thin. This is not the case however for line radiation.

2.2 Line Radiation

The energy loss per unit volume per unit time can be expressed in closed form solutions for certain geometric shapes for a given isolated line. An expression for the absorption coefficient is required however.

The classical Lorentz electromagnetic theory result corrected by quantum theory yields for the absorption coefficient, (13)

$$k_{\nu} = \frac{e^2 Nf}{m_e c} \frac{\Gamma/4\pi}{(\nu-\nu_o)^2 + (\Gamma/4\pi)^2}$$

where,

N = the number density of the excited atoms in the absorbing level

ν_o = the frequency of the bound-bound transition

f = the oscillator strength associated with the transition

Γ = the half width of the line which has been broadened.

A line exhibiting only natural and collisional broadening will be of this dispersion shape. However Doppler broadening may also be significant, and it results in a Gaussian line profile. The observed line shape is then Gaussian when this width is considerably greater than the natural and collisional broadening widths. For an intermediate case, if it is assumed that the two broadening mechanisms are statistically independent, the resulting absorption shape has the form of a "folding" integral. For this case where Doppler broadening is comparable to natural and collisional broadening, the absorption coefficient must be represented by, (14)

$$k_\nu = k_o \frac{a'}{\pi} \int_{-\infty}^{\infty} \frac{\exp(-y^2)\, dy}{a'^2 + (x' - y)^2}$$

where,

$$x' = \frac{2(\nu - \nu_o)}{\nu_o} \sqrt{\ln 2}$$

$$a' = \frac{\Delta\nu_N + \Delta\nu_c}{\Delta\nu_o} \sqrt{\ln 2}$$

$$y = \frac{2\delta}{\nu_o} \sqrt{\ln 2}$$

$$k_o = \left(\frac{\pi m_a}{2kT}\right)^{1/2} \frac{e^2}{m_e} \frac{Nf}{\nu_o}$$

At the line center where $\nu = \nu_o$, k_{ν_o} has a simple form, namely

$$k_{\nu_o} = k_o \, e^{a'^2} \, \mathrm{erfc}(a') \; .$$

For radiating argon at the test conditions it will be shown shortly that Doppler broadening is important only for resonance transitions. All the remaining transitions are broadened mainly by collisional (Stark) broadening. Since the resonance lines must be considered separately, let us presently assume that a dispersion profile describes the line shape. Making the following substitutions,

$$A^* = \frac{e^2 N f}{m_e c} \left(1 - e^{-h\nu_o/kT}\right)$$

$$B = \Gamma/4\pi$$

the expression for the absorption coefficient (dispersion) becomes,

$$k_\nu = \frac{A^* B}{(\nu - \nu_o)^2 + B^2}$$

The optical depth for the line center, then becomes,

$$\tau_{\nu_o} = (A^*/B)L$$

where L is some characteristic length. Also for radiation resulting from an isolated line,

$$B_\nu = B_{\nu_o} \; .$$

In Appendix 1 expressions for the rate of energy loss per unit volume Q are derived based on various geometries and the previously mentioned assumptions. Here only the final expressions will be presented. Three basic radiation absorption models are considered:

1. Spherical volume model (R = constant)

$$Q(\nu_o) = \frac{4\pi^2 e^2 Nf}{m_e c} B_{\nu_o} (1 - e^{-h\nu_o/kT}) e^{-\tau_{\nu_o}/2} I_o(\tau_{\nu_o}/2)$$

where

$$\tau_{\nu_o} = \frac{4\pi e^2 Nf}{m_e c \Gamma} (1 - e^{-h\nu_o/kT}) R$$

R is the effective radius of cross section of shock tube.

2. Finite circular cross section model (cylinder model)

$$Q(\nu_o) = \frac{2\pi^2 e^2 Nf}{m_e c} B_{\nu_o} \Big[ae^{-Kbx} I_o(Kbx) + ae^{-Kbx'} I_o(Kbx') - \frac{ax}{R_{cr}} e^{-KbR_{cr}} I_o(KbR_{cr}) - \frac{ax'}{R'_{cr}} e^{-KbR'_{cr}} I_o(KbR'_{cr}) + 2fe^{-Kg(L/2)} I_o(Kg\,\frac{L}{2}) - \frac{f(L/2)}{R_{cr}} e^{-KgR_{cr}} I_o(KgR_{cr}) - \frac{f(L/2)}{R'_{cr}} e^{-KgR'_{cr}} I_o(KgR'_{cr}) \Big] (1 - e^{-h\nu_o/kT})$$

where

$$K = \frac{2\pi e^2 Nf}{m_e c \Gamma} (1 - e^{-h\nu_o/kT})$$

$$(a,b) = (1, \sqrt{3})$$

$$(f,g) = (1, 5/4)$$

$$R_{cr} = \sqrt{(L/2)^2 + x^2}$$

$$R'_{cr} = \sqrt{(L/2)^2 + x'^2}$$

$$x' = h - x$$

h is distance between the ionization front and the cold front

$\frac{L}{2}$ is the radius of circular cross section .

3. Infinite domain model

$$Q(\nu_o) = \frac{2\pi^2 e^2 Nf}{m_e c} B_{\nu_o} [ae^{-Kbx} I_o(Kbx) + ae^{-Kbx'} I_o(Kbx')](1-e^{-h\nu_o/kT})$$

where the parameters K, a, b, x' are defined in case 2. In all three models I_o is the modified Bessel function of the first kind of order zero.

These closed form solutions, even though based on over simplified radiation models, exhibit the importance of absorption through optical depth. (A comparison of these models will be presented in Chapter 4.) The energy loss per unit volume per unit time for a given bound-bound transition is proportional to the oscillator strength and the number of excited atoms in the absorbing level. The uncertainty in the values for oscillator strengths helps justify the selection of the above radiation absorption models. Appendix II briefly discusses the argon atom spectra and includes an energy level diagram for argon I.

2.2.1 Optical Depth of Bound-Bound Transitions

Recall that the optical depth at $\nu = \nu_o$ is defined by

$$\tau_{\nu_o} = \frac{A^*}{B} \cdot L$$

where B is a measure of the broadening of the line, A^* is proportional to the product of the number of absorbers and the oscillator strength, and L is some characteristic length.

For a dense plasma most of the line broadening is caused by Stark effects from electric microfields produced by electrons and ions surrounding the emitting atoms. For atoms other than hydrogen (and certain helium lines) it is the second order or quadratic Stark effect which broadens the lines. In a neutral plasma the electric field is rapidly changing direction and intensity. Therefore the electric field may be considered using a probability distribution of the field. Holtsmark first considered this problem by assuming the atom is influenced by the electric field of the perturbers. Since the atom is in motion, the field keeps changing magnitude which results in a broadening and shift of the line. The quasi-static (Holtsmark) theory, which accounts for broadening due to ions, considers only electrostatic actions and neglects the effect of the motion of the ions. The contribution of ion broadening to the half width is usually less than 20% (15). The "impact" theory however assumes the radiating atom is influenced by the electric field of the perturber moving with a rapid velocity. The impacts are then well separated in time and this semi-

classical approach, which accounts for the electron contribution, results in a significant broadening of the line. Such an impact approximation can be applied provided that the average interaction is indeed weak. Assuming an interaction proportional to the reciprocal of the fourth power of the interatomic distance the expression for the half width due to electron broadening becomes, (14)

$$\Gamma_s = 38.8\ C_4^{2/3}\ V^{1/3}\ N_e$$

where V is the relative "impact" thermal velocity $= (8kT/\pi\mu)^{1/2}$ and, C_4 is the quadratic Stark constant which must be determined either by experiment or quantum mechanics. For hydrogenic atoms C_4 can be expressed by, (14)

$$2\pi C_4 = 1.6 \times 10^{-17}(n_u/Z)^6 \qquad \text{cm}^4\ \text{sec}^{-1}\ ,$$

where n_u is the principal quantum number for the upper level.

For the resonance lines (any transition to the $3p^6$ state) the next most important source of broadening is self-broadening, or resonance broadening, due to interaction with like atoms in the same quantum state.

A third source of broadening, and usually second in importance, is thermal Doppler broadening, due to the relative motion of the radiating atoms and the observer. This thermal broadening leads to an half width expression of, (16)

$$\Gamma_D = \frac{4\pi \nu_o}{c} \left(\frac{2RT \ln 2}{M}\right)^{1/2}$$

where ν_o is the frequency and M is the atomic weight of the atom. Recall however that Doppler broadening results in a Gaussian line profile, and not the previously assumed Lorentz or dispersion profile. If the half width for thermal broadening is significant compared to the pressure half widths, then the assumption of a dispersion profile is invalid.

All other mechanisms are almost always negligible for relatively dense plasmas at moderate temperatures. Thus natural line broadening is always small compared to collisional, or pressure, broadening.

The half widths resulting from Stark, resonance, Doppler, and natural broadening were calculated for selected resonance transitions, and $3p^5 4p - 3p^5 4s$ and $3p^5 3d - 3p^5 4p$ transitions. For the latter case the Stark effect constant is known (17), while in the former case it must be estimated using the known value and the hydrogenic expression for C_4 as a relative equation. Only for the resonance transitions was Doppler broadening found to be a significant contributor to the total line half width. Recall that since A^* is directly proportional to the number of absorbers, A^* is a maximum for the resonance transitions. Since a Boltzmann distribution is assumed to exist, the number density of the first excited state for argon is much smaller than the ground state population for moderate temperatures. For higher levels the population is even less. The half width term, B, has little effect

in determining the optical depth since A^* normally dominates over B. In the table below selected transitions are shown with their corresponding optical depth for typical test conditions ($T = 12000°K$, $N_e = 10^{17} cm^{-3}$, $L = 5.0$ cm).

Transition	Optical Depth
$1s_2 - 1p_o$	2.46×10^4
$1s_4 - 1p_o$	0.62×10^4
$2p_2 - 1s_2$	0.57
$2p_2 - 1s_4$	0.56

The resonance lines are indeed thick, while the $4p4s$ (and $3d4p$) lines appear to have an optical depth of the order of unity. These transitions therefore experience absorption, and one of the previously discussed radiation absorption models must be applied. Only for the case of optically thin transitions is the energy loss independent of optical depth. It must be remembered that optical depth is a function of temperature and electron and heavy particle number densities.

2.2.2 Determination of Oscillator Strengths

Recall that the spherical model yields, for the rate of energy loss per unit volume,

$$Q(\nu_o) = \frac{4\pi^2 e^2}{m_e c} B_{\nu_o} N_L f_{Lu} (1 - e^{-h\nu_o/kT}) e^{-\tau_{\nu_o}/2} I_o(\tau_{\nu_o}/2) .$$

Now assuming a Boltzmann distribution of excited states, given by

$$\frac{N_L}{N_a} = \frac{g_L}{g_o} e^{-E_{oL}/kT}$$

where g_L and g_o are the statistical weights of the excited level and ground state respectively, and using the Planck distribution function,

$$B_{\nu_o} = \frac{2h\nu_o^3}{c^2} \left(e^{h\nu_o/kT} - 1 \right)^{-1}$$

a more useful expression for the rate of energy loss per unit volume for an isolated line can be written,

$$Q(\nu_o) = \frac{8\pi^2 e^2 h}{m_e c} \nu_o^3 \; N_a \; \frac{g_L}{g_o} f_{Lu} \; e^{-E_{ou}/kT} \; e^{-\tau_{\nu_o}/2} \; I_o(\tau_{\nu_o}/2)$$

The other radiation models yield similar results only more complicated in the terms containing optical depth.

In the above equation the oscillator strength, or f number, is usually unknown. The problem then reduces to the determination of the oscillator strengths. For argon I a few f numbers are known from experiments, but generally they must be determined from theoretical studies (Coulomb approximations, Hartree-Fock calculations, or variational calculations.)

In a manner similar to the case for optical depth, the argon I spectrum can be subdivided into several regimes depending upon how the oscillator strengths are determined. The regimes chosen more or less

coincide with the optical depth regions; the measured values corresponding to the lower level transitions, while the Coulomb approximation values corresponding to the immediate and upper optically thin transitions. For the extreme upper levels a hydrogen model is selected for which an exact expression for the hydrogen oscillator strength exists.

Regime I. Experimental Values

There are thirty possible multiplet transitions from the $3p^5 4p$ level to the $3p^5 4s$ level. The absolute transition probabilities for twenty-three of these lines have been experimentally measured (18,19, 20). The discrepancies between the measurements are within the range of error $\pm$ 20-30%. These near infra-red lines are ideal for experimental investigation, because they are free from interference of neighboring lines and because they represent the strongest lines in the series. The product of the degeneracy of the lower level and the oscillator strength for these 4p-4s transitions are shown in Table 1.

The $3p^5 5p$ - $3p^5 4s$ transitions result in lines in the visible spectrum. These transitions represent lines of the second term of the series, and hence these lines are weaker but nevertheless represent important radiation loss sources. Table 2 lists the gf values for the 5p4s multiplet transition obtained from measurements (17).

TABLE 1

$3p^5 4p - 3p^5 4s$ Transitions

transition	wavelength	$g_L f_{LU}$
$2p_1 - 1s_2$	7503.87 Å	0.364
$2p_2$	8264.52	0.476
$2p_3$	8408.21	1.055
$2p_4$	8521.44	0.345
$2p_5$		....
$2p_6$		....
$2p_7$		....
$2p_8$		....
$2p_{10}$		....
$2p_2 - 1s_3$	7724.2	0.52
$2p_4$	7948.18	0.417
$2p_7$	8668	0.14
$2p_{10}$		....

TABLE 1 Cont.

transition	wavelength	$g_L f_{LU}$
$2p_1 - 1s_4$		....
$2p_2$	7272.94	0.384
$2p_3$	7383.98	0.354
$2p_4$	7471	0.12
$2p_5$	7514.65	0.306
$2p_6$	8006.16	0.240
$2p_7$	8103.69	0.792
$2p_8$	8424.65	1.028
$2p_{10}$	9658	0.12
$2p_2 - 1s_5$	6965.43	0.116
$2p_3$	7067	0.20
$2p_4$	7147	0.05
$2p_6$	7635.11	0.884
$2p_7$	7723.7	0.10
$2p_8$	8014.79	0.384
$2p_9$	8115.31	1.533
$2p_{10}$	9123	0.35

TABLE 2

$3p^5 5p - 3p^5 4s$ Transitions

transition	wavelength	$g_L f_{LU}$
$3p_1 - 1s_2$	4259.4 Å	.0098
$3p_2$	4335.4	.0028
$3p_3$	4333.6	.0065
$3p_4$	4345.2	.0021
$3p_5$		....
$3p_6$		....
$3p_7$		....
$3p_8$		....
$3p_{10}$		....
$3p_2 - 1s_3$	4181.9	.0034
$3p_4$		....
$3p_7$		....
$3p_{10}$		....

TABLE 2 Cont.

transition	wavelength	$g_L f_{LU}$
$3p_1 - 1s_4$		....
$3p_2$		....
$3p_3$		....
$3p_4$		....
$3p_5$	4198.3	.0060
$3p_6$	4266.3	.0038
$3p_7$	4272.2	.0058
$3p_8$	4300.1	.0047
$3p_{10}$		....
$3p_2 - 1s_5$		....
$3p_3$		....
$3p_4$		....
$3p_6$	4158.6	.0142
$3p_7$	4164.8	.0015
$3p_8$		....
$3p_9$	4200.7	.0143
$3p_{10}$	4251.2	.0006

Regime II. Coulomb Approximation

Except for the above mentioned transitions, experimentally measured transition probabilities are scarce indeed. Therefore a theoretical method must be employed to determine the missing f numbers. In this regime the Bates and Damgaard (21) method has been selected. (Hartree-Fock calculations have been performed for the $4s^2P$ resonance lines of argon, (22).) One might suspect that this method would be unsatisfactory for such a complex atom. However the rather scanty comparison data suggest that even for such systems the method yields useful and in some cases precise values (21).

This method was used to determine the line strength and oscillator strength for the multiplet transitions from the 4p, 5p levels to the 4s level; the 5s, 6s, 3d, 4d, 5d levels to the 4p level; and the 4d level to the 5p level. The values for the product of the degeneracy of the lower level and the f number are listed in the chart below.

Transition	$g_1 f$
$3p^5 4p - 3p^5 4s$	11.4
5p - 4s	0.2
5s - 4p	3.4
6s - 4p	0.3
3d - 4p	27.8
4d - 4p	1.5
5d - 4p	0.13
4d - 5p	44.0

Appendix 3 discusses the application of this method to the determination of argon I oscillator strengths.

Regime III. Hydrogen Model

The previous method could not be applied to the transitions between upper argon energy levels due to the enormous number of such levels present. It was therefore decided to use the hydrogen model to calculate the total loss contribution from the upper levels. The use of the results for hydrogen has a sound basis if, for given argon levels, the term energy and the principal quantum number n are related by Rydberg's elementary formula. However corrections for different multiplicity and differences in excitation energies for argon and hydrogen levels must be considered (5). For hydrogen,

$$E_n = - \frac{R_y}{n^2} .$$

For an energy of approximately - 2 ev all argon transitions can be considered to be hydrogenic.

For an optically thin transition the rate of energy loss per unit volume for a given isolated line is equal to the product of the number of the emitters, the energy associated with the transition, and the transition probability, A,

$$E_{n'n} = h\nu_{n'n} N_{n'} A_{n'n} .$$

Let $E_n^{(m)}$ represent the energy loss of lines produced by transitions from levels $n' \geq m$ to a fixed level n,

$$E_n^{(m)} = \sum_{n'=m}^{\tilde{n}} E_{n'n}$$

and let the energy loss of the lines formed by transitions to levels for which $n \geq k$ be designated by,

$$E^{(k)} = \sum_{n=k}^{\tilde{n}} \sum_{n'=n+1}^{\tilde{n}} E_{n'n}$$

where k is the lowest principal quantum number for which the hydrogenic model is valid, and $\tilde{n}$ is the maximum value of the principal quantum number. For a dense plasma $\tilde{n}$ cannot approach infinity due to electrostatic effects which terminate the series. The Debye polarization theory (23) is used to determine the maximum principal quantum number corresponding to a lowering of the ionization potential. For a plasma of approximately 10^{17} electrons cm^{-3} this theory leads to a value of $\tilde{n}$ of about ten.

Now assume these extreme upper levels are sufficiently close together so that the double summation can be replaced by two integrals (i.e., assume a continuous distribution of energy levels), (24)

$$E^{(k)} = \int_{n=k}^{\tilde{n}} \int_{n'=n+1}^{\tilde{n}} E_{n'n} \, dn \, dn' .$$

For the hydrogen atom the oscillator strength, or f number, is known from quantum mechanics. This relation is, (25)

$$f_{n'n} = \frac{2^6}{3\sqrt{3}} \frac{1}{2n^2} \left(\frac{1}{n^2} - \frac{1}{n'^2} \right)^{-3} \frac{1}{n^3 n'^3} \, g_{BB}$$

where g_{BB} is the Gaunt correction factor for bound-bound transitions. It usually differs little from unity (26).

Using this expression to determine the corresponding transition probability, and assuming a Boltzmann distribution of excited states, the form of $E_{n'n}$ becomes,

$$E_{n'n} = \frac{256\pi e^2 h R_y^3 Z^6}{3\sqrt{3}\, m_e c^3}\, e^{-\beta}\, e^{\beta/n'^2}\, \frac{1}{n^3 n'^3}\, g_{BB}\, n_a$$

where

$$\beta = h\,\frac{R_y}{kT} \quad .$$

Then after performing the double integration $E^{(k)}$ reduces simply to, (24)

$$E^{(k)} \equiv Q^{(k)}$$

$$= \frac{256\pi e^2 h R_y^3 Z^6}{3\sqrt{3}\, m_e c^3}\, N_a\, \overline{g_{BB}}\, \frac{e^{-\beta}}{4\beta} \left[\frac{1}{\beta} \left(e^{\beta/k^2} - e^{\beta/\tilde{n}^2} \right) - e^{\beta/\tilde{n}^2} \left(\frac{1}{k^2} - \frac{1}{\tilde{n}^2} \right) \right]$$

Now applying the correction for multiplicity and difference in excitation levels $Q^{(k)}$ becomes,

$$Q^{(k)} = C_2\, N_a\, \overline{g_{BB}}\, \frac{e^{-\beta}}{4\beta} \left[\frac{1}{\beta} \left(e^{\beta/k^2} - e^{\beta/\tilde{n}^2} \right) - e^{\beta/\tilde{n}^2} \left(\frac{1}{k^2} - \frac{1}{\tilde{n}^2} \right) \right]$$

$$\times \gamma\, e^{-(\langle U_A \rangle - \langle U_H \rangle)/kT}$$

where

$$C_2 = \frac{256\pi e^2 h R_y^3 Z^6}{3\sqrt{3}\, m_e c^3}$$

N_a = number of argon atoms

γ = the multiplicity factor (6 for argon)

$\overline{g_{BB}}$ = the average bound-bound Gaunt factor

$\langle U_A \rangle$ = most probable excitation energy for argon

$\langle U_H \rangle$ = most probable excitation energy for hydrogen

The above formula expresses the total energy loss per unit volume per unit time for the extreme upper level transitions in an argon plasma.

2.3 Continuum Radiation

Radiative recombination and Bremsstrahlung are the main processes which determine the continuum emission from a moderate temperature, radiating plasma. The theory for continuum radiation from such a plasma was first formulated by Unsöld (27). He extended the hydrogenic atomic absorption coefficient for photoionization to complex, nonhydrogenic atoms by introducing a correction factor which accounted for the "effective" nuclear charge of the atomic core. Despite obvious limitations this theory seems to describe reasonably well the continuum emission for argon under certain values of the unknown parameters inherent in the theory (2,7,8).

For radiative recombination (free-bound transitions) the corresponding atomic absorption coefficient for photoionization from a principal quantum level n of a hydrogenic atom is, (25)

$$\alpha_{BF}^{(\nu)} = \frac{32\pi^2 e^6 R_y Z^4}{3\sqrt{3}\ ch^3}\ \frac{1}{n^5 \nu^3}\ g_{BF}$$

where g_{BF} is the bound-free Gaunt correction factor. A result obtained by Milne relates the above absorption coefficient to the corresponding photoionization cross section by

$$\frac{\alpha_{BF}^{(\nu)}}{\theta_{pn}} = \frac{m_e^2 c^2 v^2}{\nu^2 h^2}\ \frac{g_e\ g_{0i}}{2g_n}$$

where the g's represent the degeneracies of the free electron, ground state ion, and excited atom at energy level n. Knowing the absorption coefficient is then equivalent to knowing the photoionization cross section.

The energy emitted per unit time per unit volume in the frequency range between ν and $\nu + d\nu$ and the velocity range between v and $v + dv$ is,

$$h\nu\ N_i\ N_e\ f(v,T)\ v\ \theta_{pn}\ d\nu\ dv$$

where $f(v,T)$ is the usual Maxwellian distribution function.

The total emission in the interval $d\nu$ is found by summing the above equation over all n with ν kept constant. This procedure leads to the following expression,

$$\epsilon_{pn}^{(\nu)} = \frac{64 e^6 \pi^{3/2}}{3\sqrt{6}\, m_e^{3/2} k^{1/2} c^3} \frac{Z^2 N_i N_e}{\sqrt{T}} \frac{2hR_y Z^2}{kT} e^{-h\nu/kT}$$

$$\times \sum_{n=n_0}^{\infty} \frac{g_{BF}}{n^3} \exp\left(\frac{hR_y Z^2}{n^2 kT} \right)$$

where

$$n_0 \geq (R_y Z^2/\nu)^{1/2} .$$

The above formula expresses the total emission per unit volume per unit time for free-bound, hydrogenic transitions.

The Bremsstrahlung radiation (free-free transitions) emission can be similarly determined by using the corresponding free-free atomic absorption coefficient and Kirchhoff's law,

$$\epsilon_{pp}^{(\nu)} = \frac{64 e^6 \pi^{3/2}}{3\sqrt{6}\, m_e^{3/2} k^{1/2} c^3} \frac{Z^2 N_i N_e}{\sqrt{T}} e^{-h\nu/kT} \bar{g}_{FF} .$$

The total continuum radiation emission per unit volume per unit frequency is the sum of the two terms, or

$$\epsilon_\nu = \epsilon_{pn}^{(\nu)} + \epsilon_{pp}^{(\nu)}$$

$$= \frac{64 e^6 \pi^{3/2}}{3\sqrt{6}\, m_e^{3/2} k^{1/2} c^3} \frac{Z^2 N_i N_e}{\sqrt{T}} e^{-h\nu/kT} \left[\bar{g}_{FF} + \frac{2hR_y Z^2}{kT} \bar{g}_{BF} \sum_{n_0}^{\infty} \frac{e^{hR_y Z^2/n^2 kT}}{n^3} \right]$$

where $\bar{g}_{FF}$ and $\bar{g}_{BF}$ are the average free-free and the average bound-free Gaunt factors respectively. A plot of the normalized emission as a function of frequency is shown in Fig. 1. (The normalizing constant is taken to be

$$\frac{64e^6 \pi^{3/2}}{3\sqrt{6}\, m_e^{3/2} k^{1/2} c^3} .)$$

Notice the appearance of absorption edges which characterize the hydrogenic atom.

At this stage in the derivation it is customary to replace the summation in the free-bound term by an integration above a minimum value of n. This assumption physically implies that there exists a continuous distribution of upper levels. This technique yields,

$$\sum_{n_c}^{\infty} \frac{1}{n^3} \exp\left(\frac{hR_y Z^2}{n^2 kT}\right) \simeq \frac{kT}{2hR_y Z^2} \left(\exp\left(\frac{hR_y Z^2}{n_c^2 kT}\right) - 1\right)$$

where

$$n_c = (R_y Z^2/\nu_g)^{1/2} .$$

If the free-free and free-bound Gaunt factors are then assumed to be near unity, the expression for the total continuum loss per unit volume per unit frequency reduces to,

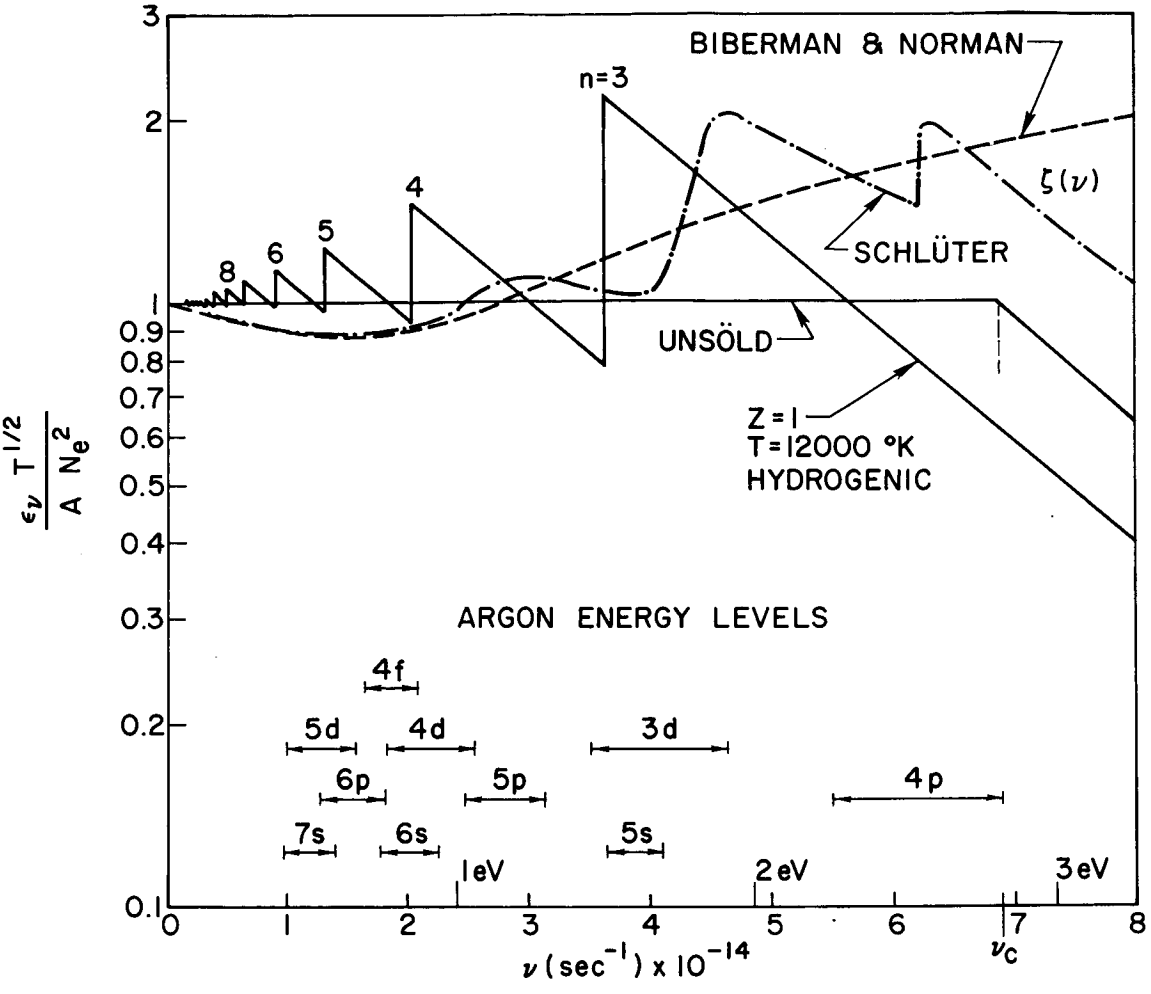

FIGURE 1 NORMALIZED CONTINUUM EMISSION AS A FUNCTION OF FREQUENCY

$$\epsilon_\nu = \begin{cases} \dfrac{64e^6\,\pi^{3/2}}{3\sqrt{6}\,m_e^{3/2}\,k^{1/2}\,c^3}\,\dfrac{Z^2\,N_i\,N_e}{\sqrt{T}} & , \quad \nu \le \nu_g \\ \dfrac{64e^6\,\pi^{3/2}}{3\sqrt{6}\,m_e^{3/2}\,k^{1/2}\,c^3}\,\dfrac{Z^2\,N_i\,N_e}{\sqrt{T}}\,e^{-h(\nu-\nu_g)/kT} & , \quad \nu \ge \nu_g \end{cases}$$

where ν_g is the critical cut-off frequency. Referring to Fig. 1 again we see that this simplification eliminates the absorption edges except for the expected exponential decay from the last level.

For nonhydrogenic atoms Z is formally replaced by the "effective" core charge, Z_{eff}, where the latter parameter is related by the hydrogenic expression,

$$E_{n,\ell} = - R_y Z_{eff}^2/n^2 \ .$$

Z_{eff} depends strongly on both n and ℓ and approaches unity for large values of n and ℓ.

Unsöld (28), Vitense (29) and others maintained that Z_{eff} could be calculated using the ground state energy. Other authors (30) have calculated Z_{eff} from average energy values based on a group of lower excited levels, and then assume Z_{eff} approached the true value of Z as the frequency decreases. Maecker and Peters (31) proposed that,

$$Z^2 < Z_{eff}^2 < n^2 \left|\frac{E_{n\ell}}{R_y}\right| \ .$$

In summary, most recent authors have chosen $Z_{eff} = 1$, but usually with some reservation. Hopefully Z_{eff} can be determined from the present experiment, at least on a consistent basis.

The cut-off frequency is related to the minimum value of the principal quantum number n_c by,

$$\nu_g = R_y Z_{eff}^2 / n_c^2 \ .$$

Petschek et al. (2), Pomerantz (3), and McChesney and Al-Attar (4) have chosen $h\nu_g$ equal 6 ev. In obtaining this value it is assumed that electron capture with energy less then $\frac{3}{2}$ kT (approx. 2 ev) to the first excited state is fairly frequent. However since ν_g is mathematically linked to n_c, the maximum value possible for argon is 4.2 ev. Calculations by Lagar'kov and Yakubov (32) of the photoionization cross sections from the first excited state (4s) in argon indicate that radiative recombination to this level is very unlikely. Therefore it seems reasonable that the cut-off frequency must correspond to $h\nu_g \leq 2.85$ ev, i.e., the 4p level (p_{10}).

Recently Biberman and Norman (9) have calculated the emission coefficient for argon without resorting to the Unsöld theory and hence the questionable Z_{eff}^2. They believe that the Unsöld formula applied to complex atoms has neither theoretical nor experimental justification. Using the quantum defect method of Seaton and Burgess with approximations, their final expression differs from the Unsöld result only in that Z_{eff}^2 is replaced by a parameter $\zeta(\nu)$, which depends strongly on frequency and possibly on temperature. Zeta can be less than unity, while Z_{eff}^2 is equal or greater than one. Schlüter (10) reconsidered the problem and eliminated certain small energy assumptions which the former authors ignored. Both Biberman and Norman

and Schlüter's zeta parameter for argon are shown in Fig. 1. The Schlüter result seems to retain absorption edges roughly corresponding to the 3d and 4p levels.

Since the form of the emission coefficient is the same whether the Unsöld result or the quantum defect result is used, only the interpretation of Z^2_{eff} must be recognized. Therefore the expression for ϵ_ν will be written in terms of Z^2_{eff} even though it can also be interpretated as the average zeta function, $\overline{\zeta(\nu)}$.

If local thermodynamic equilibrium is assumed to exist at every point in the gas, then Kirchhoff's law holds, and

$$j_\nu = B_\nu K'_\nu = 4\pi \epsilon_\nu/\rho$$

Then using the previous expressions for the emission coefficient, the optical depth for free-free and free-bound transitions can be calculated by,

$$\tau_\nu = Lk'_\nu$$

where

$$k'_\nu = K'_\nu \rho = 4\pi \epsilon_\nu / B_\nu$$

and L is a characteristic length. Figure 2 shows a plot of the optical depth as a function of wavelength for test conditions using L = 2.5 cm (the radius of the shock tube). Notice that the optical depth is much less than one except for very low wavelengths which correspond to radiative recombination to the ground state. Since such a transition is unlikely, the continuum radiation can be assumed optically thin.

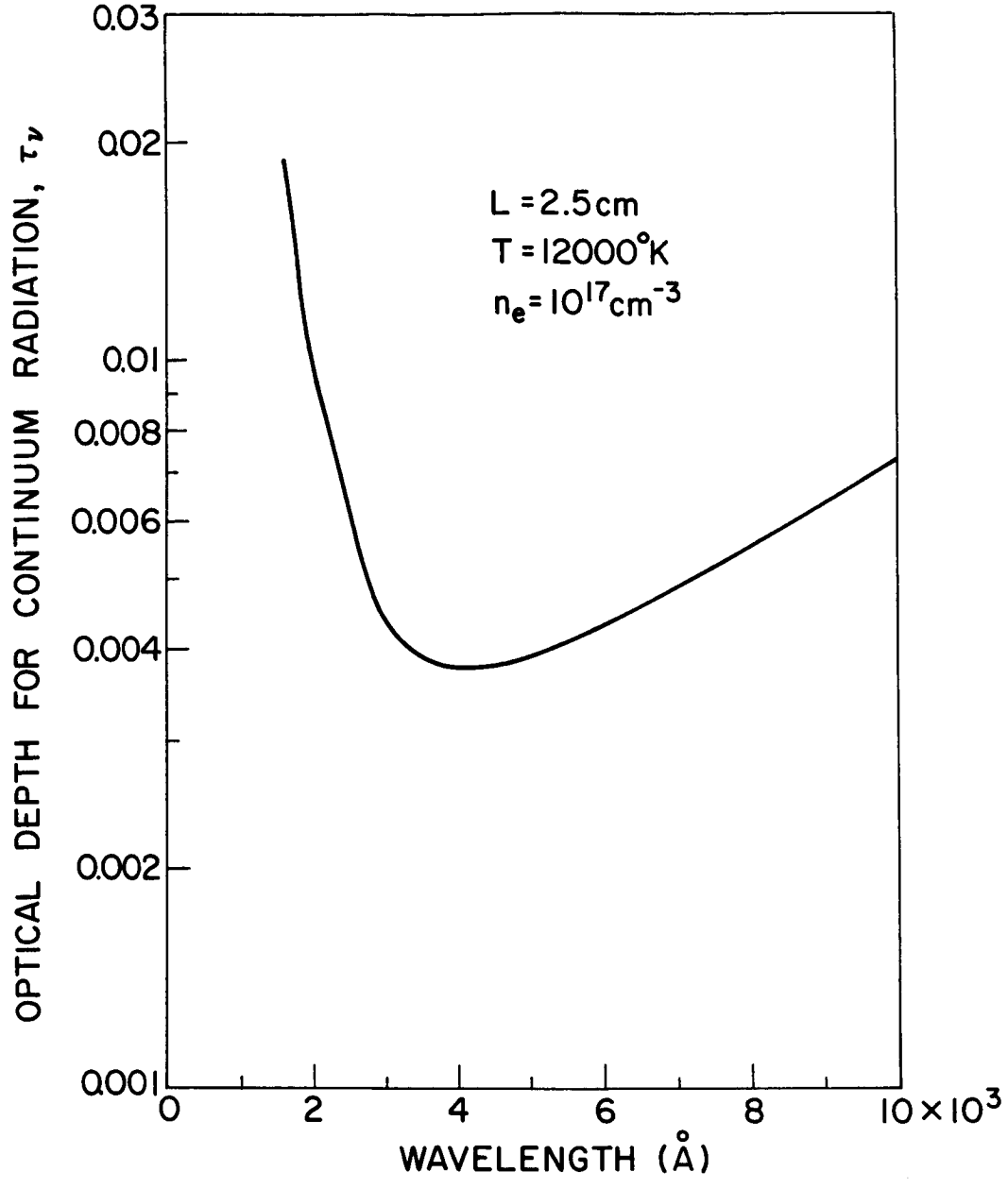

FIGURE 2 OPTICAL DEPTH FOR CONTINUUM RADIATION AS A FUNCTION OF WAVELENGTH

The energy loss per unit volume per unit time for such continuum radiation can be written as,

$$Q(c) = \int_0^\infty \epsilon_\nu \, d\nu$$

$$= \int_0^{\nu_g} \epsilon_\nu \, d\nu + \int_{\nu_g}^\infty \epsilon_\nu \, d\nu$$

$$= \frac{64 e^6 \pi^{3/2}}{3\sqrt{6}\, m_e^{3/2} k^{1/2} c^3} \frac{N_e^2}{T^{1/2}} Z_{eff}^2 \left(\nu_g + \frac{kT}{h}\right)$$

where Z_{eff}^2 and ν_g represent the unknown atomic parameters contained in the continuum theory.

2.4 Total Radiant Energy Loss

The total energy loss per unit volume per unit time is the sum of the line radiation from atomic bound-bound transitions plus the continuum radiation from free-free and free-bound transitions. Thus,

$$Q(N_e, N_a, T; x) = \sum Q(\nu_0) + Q(c) \qquad (1)$$

where

$$\sum Q(\nu_0) = Q(4p4s) + Q(3d4p) + Q(4s^2P) + Q(5p4s) + Q(6s4p) + Q(5s4p) + Q(4d4p) + Q(5d4p) + Q(4d5p) + Q(\text{upper levels}).$$

The first three terms above depend upon optical depth, or x. Bound-bound line radiation from the argon ion was not found to contribute significantly to the total radiation loss.

2.5 Governing Equations

Consider the problem of highly ionized flow behind a moving shock. Assuming no shock attenuation, this flow can be represented as steady, one-dimensional, constant area flow in shock coordinates. For inviscid flow the conservation of energy can be expressed by,

$$\rho u \frac{d}{dx} (h + u^2/2) = - Q(N_e, N_a, T; x) \qquad (2)$$

where Q is the previously determined rate of radiant energy loss per unit volume. The gas enthalpy then is,

$$h = \frac{5}{2} (1 + \alpha)RT + \alpha R\theta + RT^2(1 - \alpha) \frac{\partial}{\partial T} (\ln z_A^{el}) + RT^2\alpha \frac{\partial}{\partial T} (\ln z_i^{el})$$

for the atoms, ions, and electrons in equilibrium at the same translational temperature where θ is the ionization temperature and α is the degree of ionization. The electronic partition function can be written as

$$z_{A,i}^{el} = \sum_n g_n \exp(-\epsilon_n/kT) \quad .$$

The above summation formally extends over all the available energy levels. However this leads to the fundamental problem of its divergence since the degeneracy is proportional to n^2. This series must therefore be terminated. Numerous cutoff procedures have been suggested which are based on nearest neighbor models or electrostatic effects. The latter effect manifests itself in the form of two related

corrections, that of lowering of the ionization potential as well as partition function cutoff. Recall that in the previous section the Debye polarization term was selected to account for the lowering of the ionization potential. Assuming a cutoff based on such a lowering for temperatures below 14000°K the upper energy levels play an unimportant role, and the partition functions for argon atom and argon ion can be approximated by their ground state degeneracies, namely,

$$z_a^{el} = 1$$

$$z_i^{el} = 4 + 2 \exp(-2062/T) \ .$$

Since the argon ion has two ground states both must be included in the partition function. Then for such a temperature range the gas enthalpy reduces simply to,

$$h = \frac{5}{2} (1 + \alpha)RT + \alpha R\theta$$

since the derivatives of the log of the partition function are essentially zero. It is important to remember that the upper states are indeed assumed to play an active role in radiation losses, but due to the cutoff of the partition function and the temperature range their contribution to the enthalpy is negligible.

If the collisional rate processes dominate over the radiative processes, then local thermodynamic equilibrium can be expected to exist. One must only consider equilibration between the ground state

and the first excited state. If these populations are indeed governed by a Boltzmann distribution based on the electron temperature, then the remaining upper levels likewise exist in equilibrium. The radiative population rate between the first excited state of argon (4s) and the ground state is given by,

$$\left.\frac{dN_a}{dt}\right)_{rad} = A(2,1)\ N(2)$$

if the transition is assumed optically thin. This assumption is unlikely but results in the maximum rate. Near equilibrium the population of the first excited level can be expressed as,

$$N(2) = g(2)\ N_a\ \exp(-E_{ex}/T_e)$$

where E_{ex} is the excitation temperature and T_e is the electron temperature. Then the rate becomes,

$$\left.\frac{dN_a}{dt}\right)_{rad} = A(2,1)\ g(2)\ N_a\ \exp(-E_{ex}/T_e)\ .$$

The collisional population rate near equilibrium is practically equal to the collisional excitation rate to the first excited state. Using the excitation rate constant developed by Petschek and Byron (33) from inelastic cross section data for electron-atom collisions, the collisional rate is given by

$$\left.\frac{dN_a}{dt}\right)_{coll} = k_I\ N_e\ N_a$$

where $k_I = 3.78 \times 10^{-16}\ T_e^{3/2}\ e^{-E_{ex}/T_e}\ (2 + E_{ex}/T_e)\ cm^3\ sec^{-1}$.

Assume the criteria for the existence of equilibrium is,

$$\left.\frac{dN_a}{dt}\right)_{coll} > 10 \left.\frac{dN_a}{dt}\right)_{rad} .$$

Then solving for N_e using the two rate expressions yields,

$$N_e > 1.1 \times 10^{24}/(2 + E_{ex}/T_e)\ T_e^{3/2} .$$

For an argon plasma at $T_e = 12000°K$, an electron density of $N_e > 6 \times 10^{16}\ cm^{-3}$ is required for the radiative rate to be negligible compared to the collisional rate. Since under these test conditions the resonance lines are strongly reabsorbed the above criteria can be somewhat relaxed, and thus a slight decrease in the electron density is permissible to guarantee the existence of complete local thermal equilibrium.

Thus for a dense plasma as in the present experiments where the electron density is of the order of 10^{17}, it is safe to assume the gas remains in successive equilibrium states upon cooling. This means that the previously assumed Boltzmann distribution of excited states exists in the radiation loss region. Recent experiments performed in mercury gas verify this assumption (34). The justification of the assumption of local thermodynamic equilibrium allows one to use the Saha equation instead of the awkward and sometimes questionable rate equation. The Saha equation relates the equilibrium degree of ionization to the

local pressure and temperature by,

$$\frac{\alpha^2}{1 - \alpha^2} = \left(\frac{2\pi m_e}{h^2} \right)^{3/2} \frac{2z_i^{el}}{z_a^{el}} \frac{(kT)^{5/2}}{p} \exp(- [\theta - \Delta\theta]/T) \ . \qquad (3)$$

The three remaining equations which are needed to fully describe the flow field are the conservation of mass, the conservation of momentum, and the equation of state for a partially ionized gas. They have the usual form in shock coordinates,

$$\rho u = \rho_1 u_1 \qquad (4)$$

$$P + \rho u^2 = P_1 + \rho_1 u_1^2 \qquad (5)$$

$$P = (1 + \alpha)\rho RT \qquad (6)$$

where

$$\alpha = \frac{N_e}{N_e + N_a} \ .$$

In the momentum equation above the radiation pressure term is neglected.

The set of five governing equations (2), (3), (4), (5), and (6) plus the expression for the rate of energy loss per unit volume is solved numerically on an IBM 7090 computer. The solution gives the flow variables as a function of laboratory time relative to the end of the equilibrium region behind the incident shock.

3. EXPERIMENTAL METHOD

3.1 Application of Interferometry to the Study of Radiation and Recombination Phenomena

Alpher and White (35) first investigated the feasibility of using interferometry as a diagnostic tool for determining the electron density through measurements of optical refractivity. A Mach-Zehnder interferometer is suitable for such optical refractivity measurements.

For a partially ionized gas composed of ground state atoms, ions, and free electrons, the refractive index becomes, (1)

$$n = 1 + 2\pi(a^{+}N_i + a^{o}N_a) - \frac{1}{2}\left(\frac{\omega_p}{\omega}\right)^2$$

where

ω_p = the plasma frequency = $(4\pi N_e e^2/m_e)^{1/2}$

ω = the impressed frequency = $2\pi\nu$

a^{+} = polarizability of the ion

a^{o} = polarizability of the atom (ground state)

N_i = number density of ions

N_a = number density of atoms (ground state)

N_e = number density of free electrons.

This expression is valid when the collision frequency is much less than the impressed frequency, $(\nu_c/\omega) \ll 1$, and when the number density of the excited atoms is small compared to the ground state atom number density.

The change in the refractive index between two regions (1 and 2) for a homogeneous optical path length is related to the dimensionless shift in interferometric fringes by, (1)

$$n_2 - n_1 = \lambda\delta/L$$

where,

L = the optical path length (width of shock tube)

λ = the impressed wavelength

δ = the dimensionless fringe shift.

If N_t represents the number density of the ground state atoms directly behind the incident shock where the degree of ionization is zero, the number densities of the atoms, ions, and electrons at any point become respectively,

$$N_a = N_t(1 - \alpha)$$
$$N_i = N_t\alpha$$
$$N_e = N_t\alpha$$

and,

$$N = N_t(1 + \alpha) = \text{total number density} .$$

Then the refractive index for each of the two regions can be written as,

$$n_2 - 1 = 2\pi\rho_2 \left[a^+\alpha_2 + a^o(1 - \alpha_2) - \frac{1}{m_e}\left(\frac{e\lambda}{2\pi c}\right)^2 \alpha_2\right]$$

$$n_1 - 1 = 2\pi\rho_1 \left[a^+\alpha_1 + a^o(1 - \alpha_1) - \frac{1}{m_e}\left(\frac{e\lambda}{2\pi c}\right)^2 \alpha_1\right] .$$

Then the expression for the dimensionless fringe shift becomes,

$$\delta = \frac{L}{\lambda}\ (n_A - 1)_0 \frac{\rho_1}{\rho_0}\left[\left(\frac{\rho_2}{\rho_1} - 1\right) + \alpha_2 \frac{\rho_2}{\rho_1}\left(\frac{a^+}{a^o} - \frac{1}{m_e}\left(\frac{e\lambda}{2\pi c}\right)^2 - 1\right)\right.$$

$$\left. - \alpha_1 \left(\frac{a^+}{a^o} - \frac{1}{m_e}\left(\frac{e\lambda}{2\pi c}\right)^2 - 1\right)\right]$$

where

$(n_A - 1)_0$ = the reduced refractive index of argon evaluated at standard temperature and pressure (T_0, P_0)

$$= a^o \frac{2\pi P_0}{R m_a T_0}$$

and

$$\frac{a^+}{a^o} = 0.67 \quad (36) \ .$$

Table 3 lists $(n_a - 1)_0$ as a function of impressed wavelength in the visible spectrum for ground state argon.

For the atoms and ions the fringe shift is inversely proportional to the impressed wavelength, while for the electrons the shift is directly proportional. The latter effect is due to the index of refraction for free electrons being less than unity. Partial and total fringe shifts are shown in Fig. 3 for the equilibrium conditions corresponding to the end of the relaxation zone as a function of incident Mach number for an initial pressure of 5 mm Hg. and an impressed wavelength of 5890 Å. Notice that the electron partial fringe shift predominates for strong shocks. Thus the sensitivity of the interferometric method depends on the Mach number, or really the electron density,

TABLE 3

Refractivities of Argon

$\lambda(\mathring{A})$	$(n_A - 1)_0 \times 10^4$	Reference
4109	2.869	H
4280	2.866	H
4358	2.864	H
4801	2.838	L-B
4917	2.841	H
5087	2.831	L-B
5110	2.841	H
5210	2.828	L-B
5220	2.838	H
5460	2.837	H
5461	2.835	H
5462	2.823	L-B
5677	2.825	H
5700	2.830	H
5770	2.831	H
5771	2.817	L-B
5783	2.825	L-B
5792	2.817	L-B
5876	2.827	H
5983	2.820	H
6440	2.809	L-B
6560	2.820	H
6564	2.814	H
6760	2.778	L-B

Hall, J.G., "Shock Tubes", Part II, UTIA Review No. 12 Landolt-Bornstein, Springer-Verlag, V. II, Part 8, 1962.

$N_e = 10^{16}$ cm^{-3} is considered the minimum electron density for which this technique is applicable. Measurements result in an uncertainty of approximately 0.1 fringes. This corresponds to an experimental accuracy of several percent for electron densities of the order of 10^{17} cm^{-3}.

3.2 Experimental Apparatus

A conventional combustion drive shock tube was used to generate the dense argon plasma (Fig. 4). The two inch square, twenty five feet long, driven section was extruded from aluminum stock. A stainless steel driver section with an internal diameter of three inches and three quarter inch walls permitted combustion drive. A combustible mixture of oxygen, hydrogen, and helium was ignited by a spark ignition system, which utilized regular motorcycle spark plugs. Prescribed aluminum diaphragms separated the combustion driver from the driven section. The depth of the scribe and the initial upstream loading pressure (100 to 400 psi) determined the resulting shock speed. A mercury diffusion pump vacuum system evacuated the driven section to a prefilling pressure of approximately 10^{-5} mm Hg., as recorded by an ionization gauge. Initial pressures ranged between two and ten mm Hg. of regent grade Linde argon. Heating tapes were utilized periodically to outgas the system, while acetone and alcohol cleaning agents were used frequently to cleanse the interior shock tube walls. A dump tank, separated from the test section by a thin prescribed

aluminum diaphragm, prevented the formation of a reflected shock wave. Testing time resulted in the order of 100 microseconds, although only twenty microseconds were usually utilized for interferometric testing. A schematic drawing of the shock tube facility and the associated instrumentation is shown in Fig. 5.

Three barium titanate pressure transducers mounted flush to the interior wall of the test section served as measuring stations. Signals from these transducers were recorded on a dual beam oscilloscope. Figure 6 illustrates the technique employed and shows a typical oscillogram. Transducer 1 triggered the oscilloscope and the other auxiliary equipment such as the time delay unit and light source. The time interval between stations 2 and 3 yielded the shock speed. The initial temperature was recorded by a mercury thermometer placed in contact with the exterior wall near the test section. The resulting error in Mach number was of the order of $\Delta M/M = 0.03$ when transducer 1 was used as a third measuring station. The corresponding error in gas temperature was of the order of $\Delta T/T = 0.02$. Thus there was no noticeable shock attenuation between the three measuring stations.

A Wallace and Tierman 0-50 mm Hg. vacuum gauge, calibrated by a McLeod mercury manometer, measured the initial pressure p_1. Errors in the pressure reading were estimated to be of the order of,

$$0.06 < \Delta p_1/p_1 < 0.04$$

for the 2 mm Hg. to 10 mm Hg. test range.

The Mach-Zehnder interferometer is shown in Fig. 7 while a schematic drawing of the interferometric system is shown in Fig. 8.

This interferometer was on loan through the courtesy of the Lockheed Missiles and Space Company Research Laboratory. Since the field size diameter was greater than two inches, the whole flow could be observed. The test section housed two 2.75 inch diameter optical quality windows with a matching pair located in the compensating section of the interferometer. The 0.75 inch borosilicate crown glass windows were ground flat to 1/4 wavelength and parallel to 0.0005 inches.

An exploding wire was used as a high intensity light source. This setup resulted in approximately twenty microseconds of near continuum light. The system was triggered by a spark gap initiated by break down from a thyratron unit. This setup yielded a consistent time delay of less than three microseconds.

The time resolved interferograms were recorded on a rotating mirror camera, which utilized a hexagonal stainless steel mirror with faces ground flat to 1/2 wavelength (Fig. 9). The mirror, driven by an air turbine motor, swept an image of a vertical slit of 0.002 inches at a writing speed of approximately 2.5 mm per microsecond. This photographic technique resulted in a time resolution of less than 0.2 microseconds. For certain tests (as explained in Appendix 4) "snap shot" interferograms were desired. For these tests a Kerr Cell unit was incorporated as an electronic shutter. Such a system was required since radiating argon tended to overexpose the Polaroid film. For these experiments a two microsecond exposure time was selected.

Since fringe shifts were required at two wavelengths, the flow field was normally split using two interference filters. The filters

chosen were 4500 Å and 5890 Å, each having a band width of approximately 90 Å. These filters were located at the image plane of the test section. Greatest sensitivity was obtained with the widest spread in difference in wavelength. The two wavelengths selected had the advantage that they were isolated from strong lines of argon I while they retained a relatively large spread in wavelength.

Time integrated spectrograms were recorded on a Hilger quartz prism spectroscope, using Kodak F-1 photographic plates (2500 Å to 6800 Å). The continuum emission from the radiating argon gas was recorded on a filtered photomultiplier system.

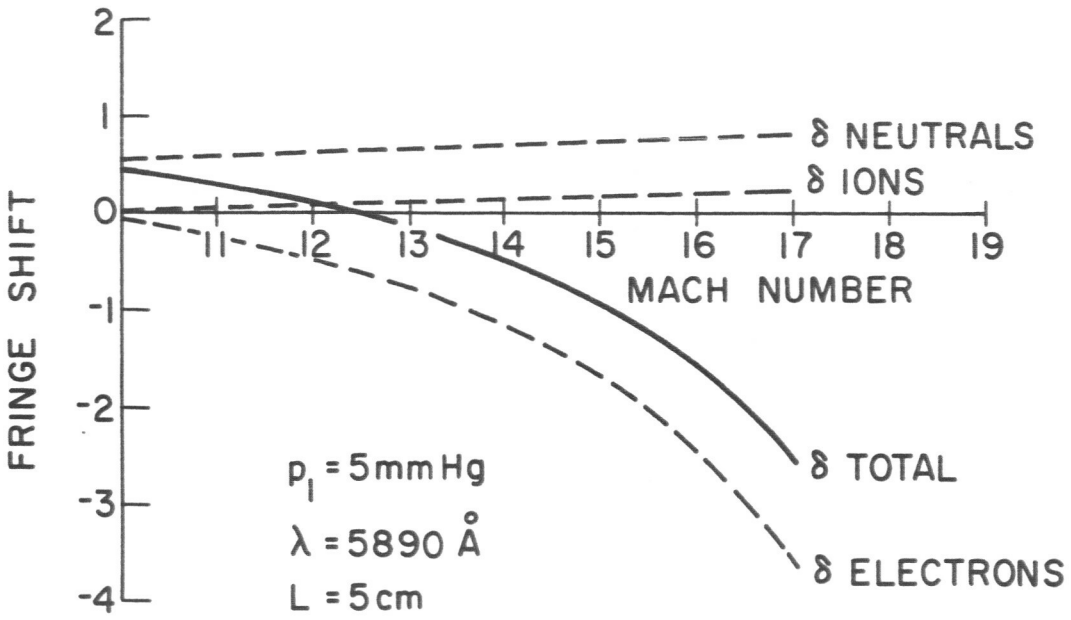

FIGURE 3 PARTIAL AND TOTAL EQUILIBRIUM FRINGE SHIFTS RELATIVE TO CONDITIONS AHEAD OF THE SHOCK AS A FUNCTION OF MACH NUMBER

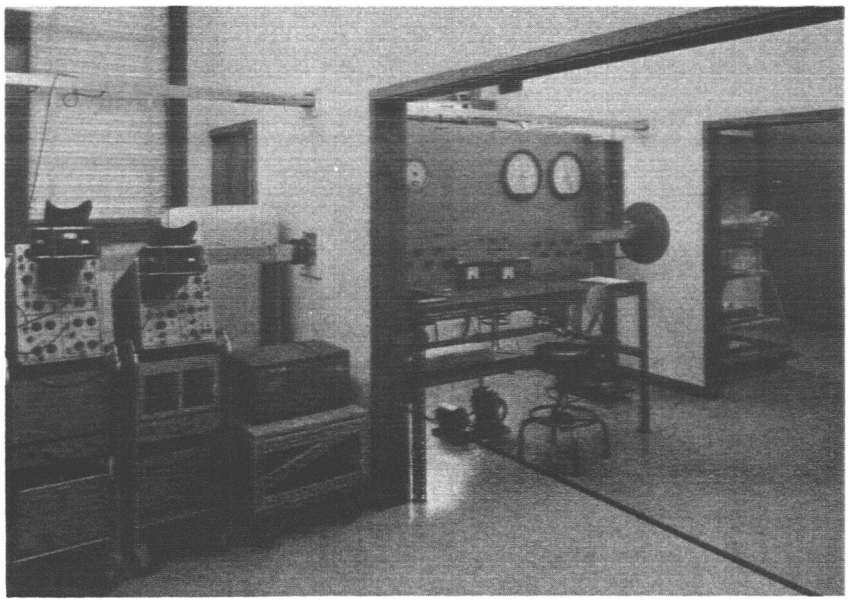

FIGURE 4 SHOCK TUBE FACILITY

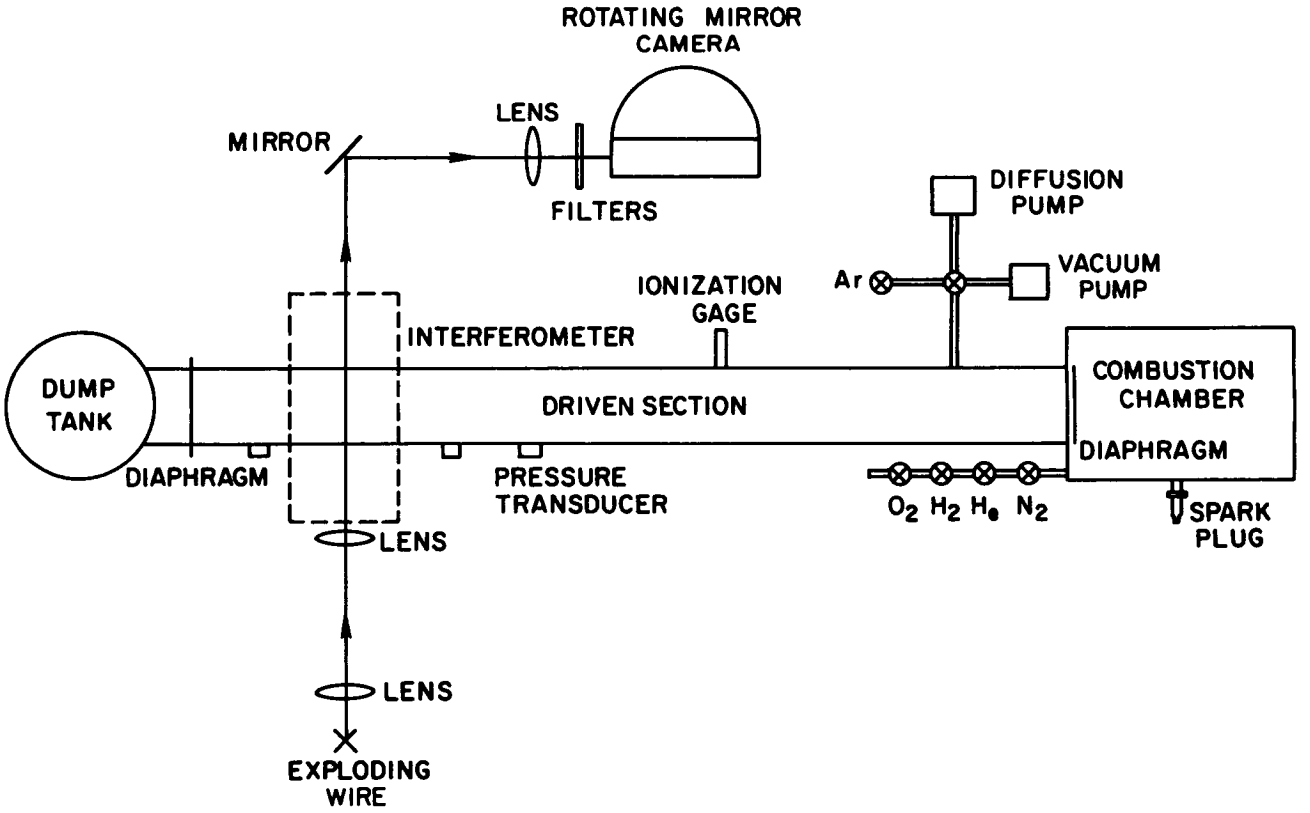

FIGURE 5 SCHEMATIC DRAWING OF THE SHOCK TUBE

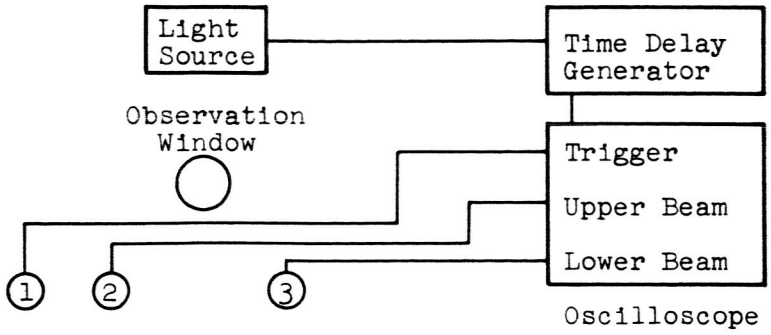

SCHEMATIC DIAGRAM OF ELECTRIC SYSTEM

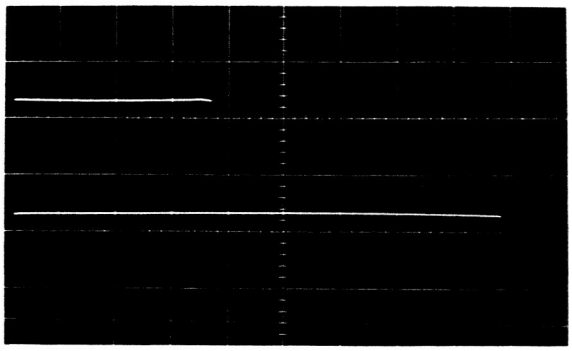

OSCILLOSCOPE TRACE

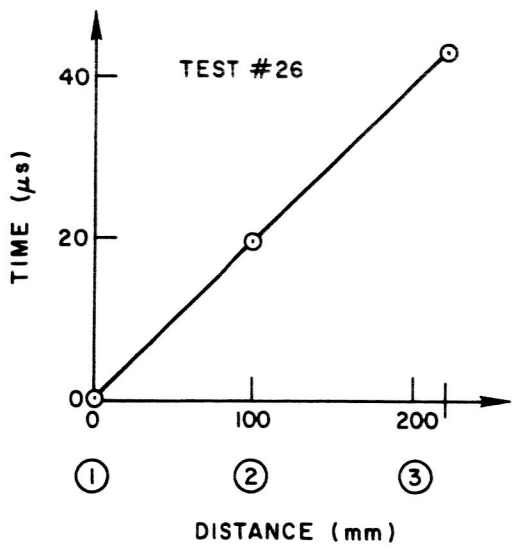

FIGURE 6 RECORD OF SHOCK SPEED MEASUREMENT

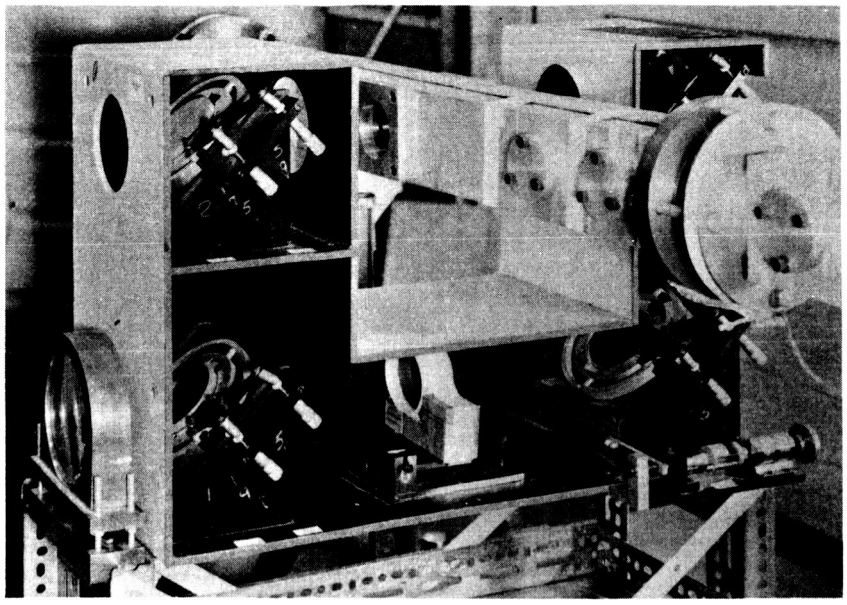

FIGURE 7 MACH-ZEHNDER INTERFEROMETER

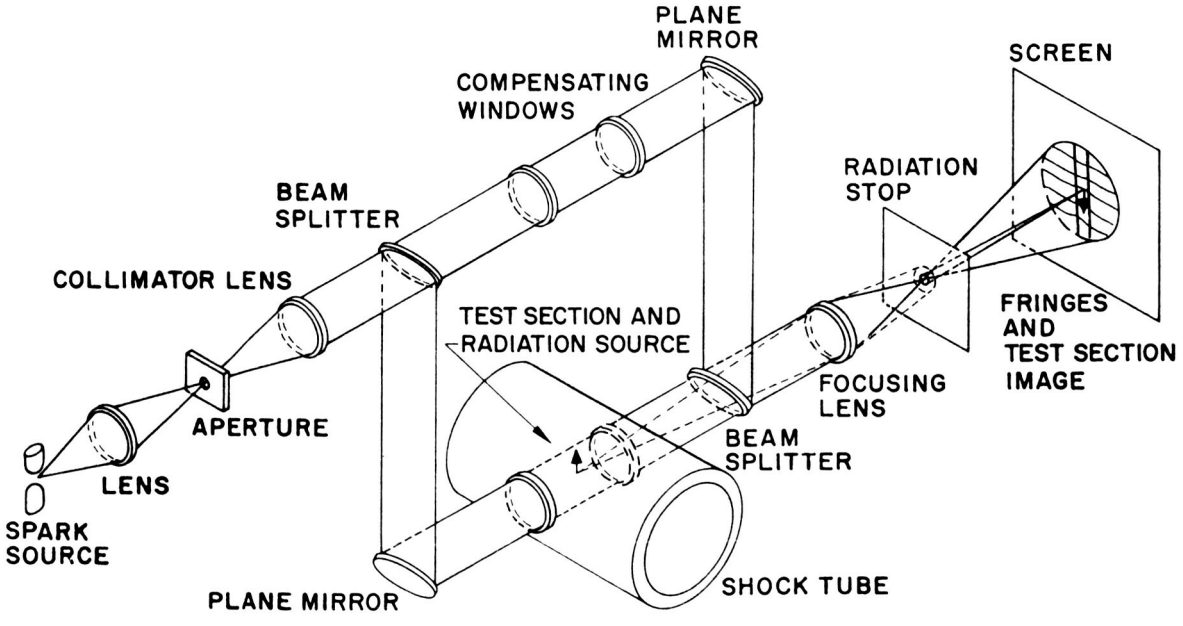

FIGURE 8 SCHEMATIC DRAWING OF THE INTERFEROMETRIC SYSTEM

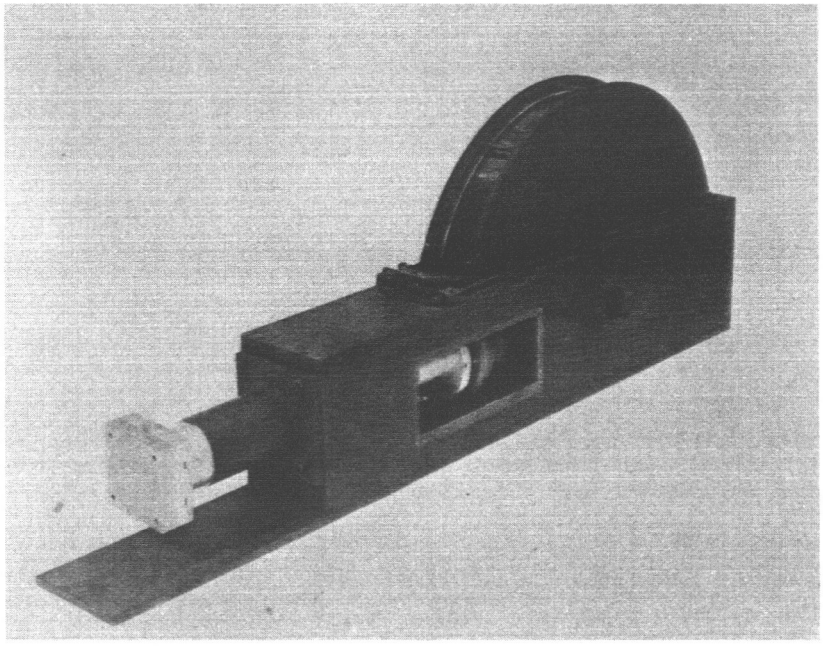

FIGURE 9 ROTATING MIRROR CAMERA

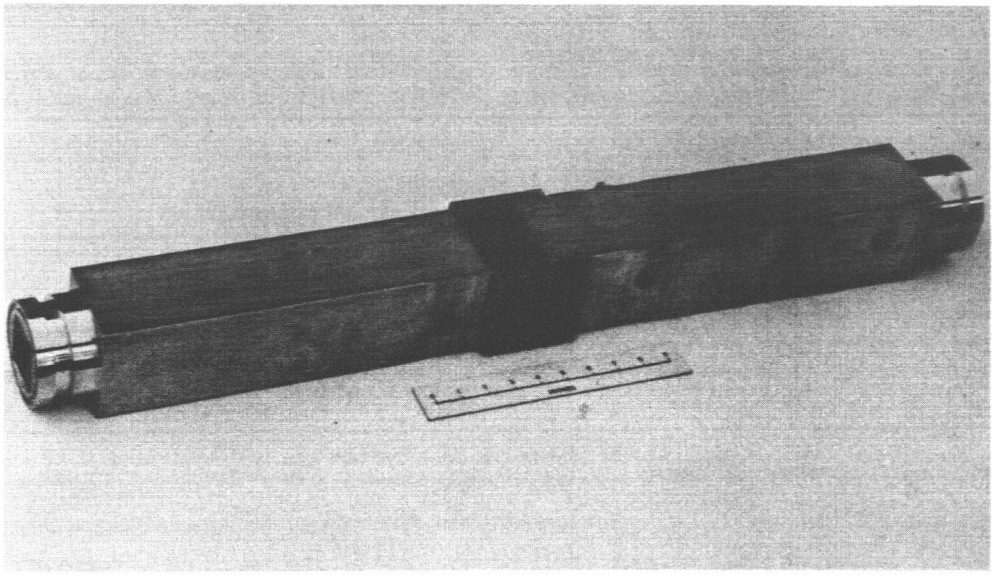

FIGURE 10 TEST SECTION

4. EXPERIMENTAL RESULTS AND DISCUSSION OF RADIATION LOSSES

4.1 Examples of Data and Early Conclusions

Rotating mirror camera interferograms of the flow behind the incident shock wave were obtained for the following test conditions:

M_s	p_1 (mm Hg)	T_1 (°K)
19.3	2	298.0
16.3	3	296.0
17.8	3	296.0
18.0	3	296.5
14.9	5	296.0
15.6	5	293.8
15.7	5	296.0
16.3	5	296.0
13.05	10	296.0

From measurements of the fringe shifts at two wavelengths a time history of both the electron density and heavy particle density was experimentally determined. Figures 11, 12, and 13 show interferograms for three of the above test conditions. Each interferogram exhibits the same flow characteristics, namely, at the shock front the fringes are shifted upwards due to the sudden increase in heavy particle density. This initial shift agrees with the predicted value when only the translational modes of the gas are considered. Notice that the initial jump in fringes is greater for the shorter wavelength,

since the partial fringe shift for the heavy particles is inversely proportional to wavelength. The subsequent production of electrons, first through atom-atom inelastic collisions and then electron-atom inelastic collisions, causes the fringes in both wavelengths to shift downwards, thereby indicating the index of refraction is controlled predominately by the free electrons. The maximum negative fringe shift agrees with the value predicted using the Saha equation. This result has been previously observed by several investigators (1, 35). For strong shock conditions the Saha equilibrium state corresponds to a transient condition however, as the fringes in both wavelengths then begin to slope upwards. This upwards shift in fringes with time indicates the presence of a loss mechanism. In the earlier photometric studies (2,6,7,8) this loss was attributed to free-free and free-bound continuum emission. Visible radiation resulting from some radiative process is observed on the interferograms starting near the end of the relaxation zone.

First assuming a continuum loss emission the set of governing equations was solved numerically for the degree of ionization as a function of laboratory time. Figure 15 shows a comparison of the experimental data with the continuum theory for the $M_s = 16.3$, $p_1 = 5$ mm Hg test. Note that zero time corresponds to the end of the relaxation zone ($t_{relax} \sim 3$ microseconds). First observe that such radiation losses result in an appreciable reduction in the degree of ionization and hence the gas enthalpy. Two theoretical curves corresponding to two different values of the parameter Z^2_{eff} are shown on this figure. For the continuum parameter equal to 2.72 there appears to be good

agreement between theory and experiment. The double pointed arrow indicates the experimental uncertainty, assuming an error of 0.1 fringes.

Since the main source of continuum radiation from a one ev plasma is radiative recombination to the upper excited levels, and since these upper levels of argon are close to being hydrogenic, that is they follow the Rydberg formula, one must conclude that, if the continuum theory applies for radiating argon, the value for the effective nuclear charge parameter should be closer to unity than to 2.72. Recall that the average value of the zeta function of Biberman and Norman and of Schlüter is well below 2.72.

The possible importance of line radiation is also indicated by the presence of strong $5p^4s$ spectral lines on the time integrated spectrograms. A typical spectrogram is shown in Fig. 14. All of the recorded spectral lines are identified as argon I transitions. The lack of impurity lines could be attributed to the relatively large f number of the spectroscope and to the limited spectral range of the photographic plates (F-1). The use of regent grade argon and the low initial evacuation pressure resulted in an impurity level estimated to be less than twenty parts per million.

Hence the presence of strong spectral lines and the unusually large value of Z_{eff}^2 necessary to correlate the data with the continuum theory suggest the fact that line radiation might be a significant contributor to the total energy loss.

4.2 Inclusion of Line Radiation

In section 2.4 an expression for the total radiant energy loss per unit volume per unit time for both continuum and line radiation was presented. Ten terms, three of which considered possible absorption, accounted for the contribution by line radiation. The resonance lines ($4s^2P$) under test conditions were optically thick, while the $4p4s$ and $3d4p$ transitions were neither thick nor thin since their optical depth was approximately one. In order to accurately estimate the loss of these lines absorption had to be considered by using the previously derived radiation absorption models (section 2.2). For the $M_s = 16.3$, $p_1 = 5$ mm Hg test conditions the set of governing equations was numerically solved yielding the fraction of radiant energy loss from the $4p4s$ transitions as a function of laboratory time for the three absorption models--a sphere of constant radius, an infinite domain, and a finite domain of circular cross section. These three absorption models are illustrated in the sketch on page 65.

Figure 16 shows a plot of the resulting relative loss for such transitions normalized by the total energy loss including continuum and all possible line radiation. Since the sample of radiating gas is bounded on one boundary by the "ionization" front for all radiation models except the first, the sphere of constant radius, maximum loss occurs at this ionization" front. This is because at such a boundary the characteristic length which determines the optical depth is zero in shock coordinates, and the radiation appears optically thin. For these test conditions the contribution of energy loss from the $4p4s$

lines to the total energy loss is approximately 30%. As the point in question, x_0, increases in shock coordinate distance, the loss from these lines decreases. As expected minimum loss corresponds to the infinite domain model, since an imaginary infinite gas extent is assumed. Likewise the spherical model results in the maximum loss, since absorption is possible only within a sphere whose radius approximates the effective radius of the cross section of the shock tube. These two models represent the two limiting cases, while the finite circular cross section model most closely approximates the actual shock tube geometry. In this case the radiating gas is bounded between the "ionization" front and the "cold" front. The theoretical curve for this absorption model lies between the two limiting cases as shown in Fig. 16. Since the constant radius spherical model always assumes an imaginary radiating gas volume even at $t = 0$, this absorption model fails to demonstrate the characteristic rapid change in optical depth and results in a nearly uniform loss dependence with time.

Recall that anticipation of slow cooling rates constituted the fundamental assumption in deriving the absorption models of Chapter 2. Figure 17 shows a plot of temperature as a function of laboratory time for two test conditions. The local temperature is normalized by the Saha equilibrium value corresponding to $t = 0$. Notice that in both cases the temperature ratio is a slowly varying function of time; the maximum decrease being less than 5% of the initial value after ten microseconds. This result helps justify the selection of a local constant temperature model.

In Figures 18, 19, 20 and 21 degree of ionization is shown as a function of laboratory time for four tests where the circles represent experimentally determined values. Zero time again corresponds to the end of the electronic relaxation zone. In Figure 18 three theoretical absorption model curves representing the infinite domain, the finite circular cross section domain, and the constant radius spherical domain are shown. Under the assumed set of continuum theory parameters fair agreement is found between the experiment and the theory for all three models. Only for longer testing times would the choice of the model become critical. It is important to remember however that some absorption model must be incorporated, for considering the 4p4s and 3d4p lines as optically thin results in unusually large losses. Thus for the limited range of optical depth encountered ($\tau_{\nu_o} < 1$) the spherical model sufficiently accounts for the absorption effects. Simplification then results in the numerical solution since the expression for the rate of the energy loss per unit time, Q, is no longer a function of distance, x_0.

The critical cutoff frequency is chosen to correspond to $h\nu_g = 2.85$ ev. This value refers to a transition from the ionization limit to the $4p(p_{10})$ level. ν_g and Z^2_{eff} are related; the smaller ν_g the closer Z^2_{eff} approaches unity. For all nine tests good agreement is found to exist for a value of the effective nuclear charge of 1.5. The Biberman and Norman, and Schlüter average zeta function has a value close to 1.5 for $h\nu_g = 2.85$ ev. Therefore a consistent and realistic set of continuum theory parameters results.

Figures 22 and 23 show the distribution of the fraction of radiant energy loss as a function of time for two tests with the same Mach number but different initial pressures. Notice that the contribution to the total loss is approximately equal for both continuum emission by free-bound radiative recombination and line radiation. The 4p4s and 3d4p transitions represent the main line sources even though they experience absorption. (For this analysis the choice of the absorption model is critical!) Also notice that the accumulative effect of the remaining spectral lines cannot be neglected, as they represent approximately 20% of the total loss.

For a given shock Mach number the higher the initial pressure the larger the absolute continuum emission and the larger the relative continuum loss contribution. The former statement is valid since the higher pressure results in a larger electron density, while the latter statement is also valid since the higher pressure results in optically thicker 4p4s and 3d4p transitions. In Figures 18 and 19 the first result is demonstrated by noting the slope of the experimental curves of degree of ionization, while the second result is shown by Figures 22 and 23.

The Debye polarization theory used to terminate the upper excited level led to a maximum principal quantuum number $\tilde{n}$ of approximately 10. Figures 22 and 23 show that the energy loss resulting from these hydrogenic levels is approximately ten percent of the total loss. The actual value for the maximum principal quantum number is inconsequential, for letting $\tilde{n}$ approach infinity results in an

increased loss by these levels of only several additional percent. The loss from the intermediate level transitions of argon I, determined using the Bates and Damgaard approach (referred to as "other lines" in Figures 22, 23) also represents approximately ten percent of the total loss.

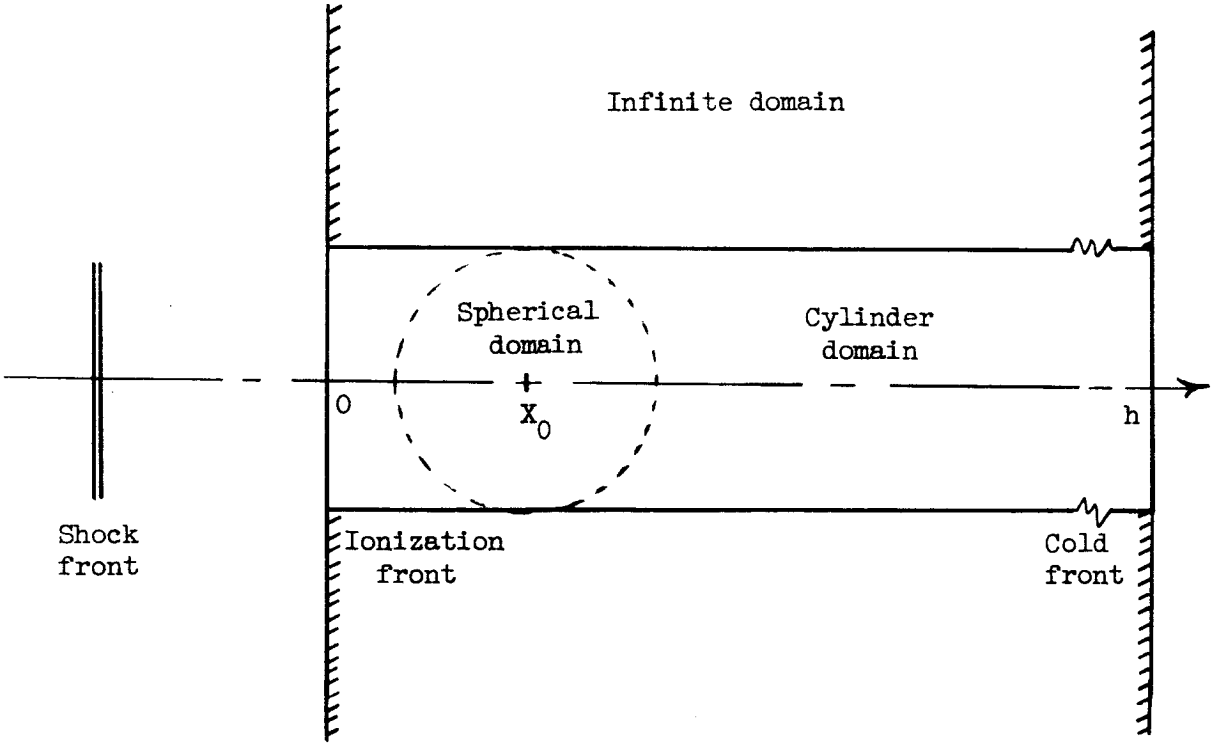

Radiation Absorption Models

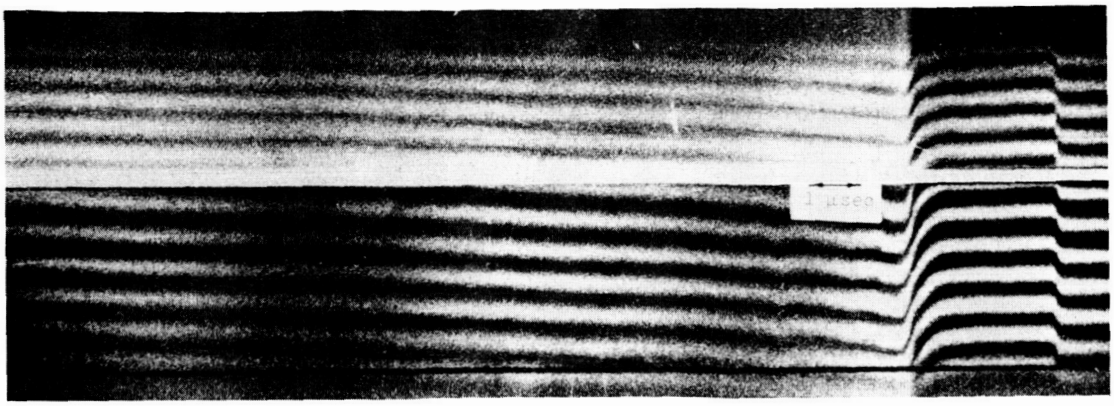

FIGURE 11 ROTATING MIRROR CAMERA INTERFEROGRAM
($M = 16.3$, $p_1 = 5$ mm Hg, $T_1 = 296.0°K$)

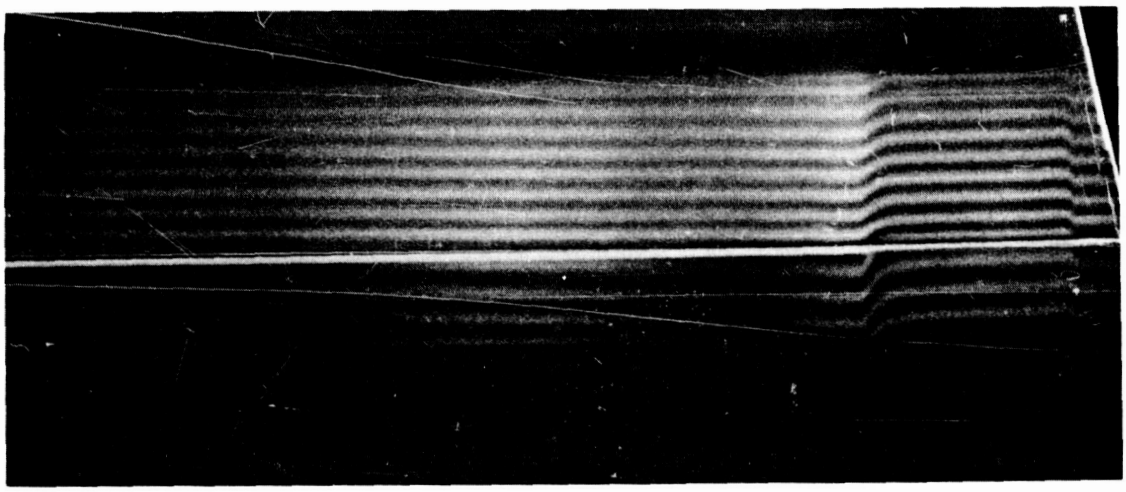

FIGURE 12 ROTATING MIRROR CAMERA INTERFEROGRAM
($M = 16.3$, $p_1 = 3$ mm Hg, $T_1 = 296.0°K$)

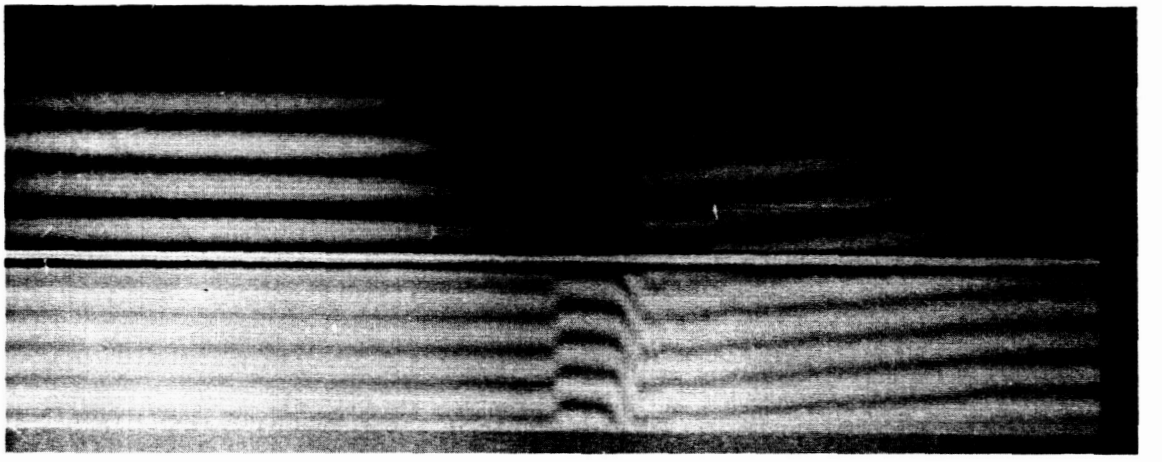

FIGURE 13 ROTATING MIRROR CAMERA INTERFEROGRAM
($M = 18.0$, $p_1 = 3$ mm Hg, $T_1 = 296.5°K$)

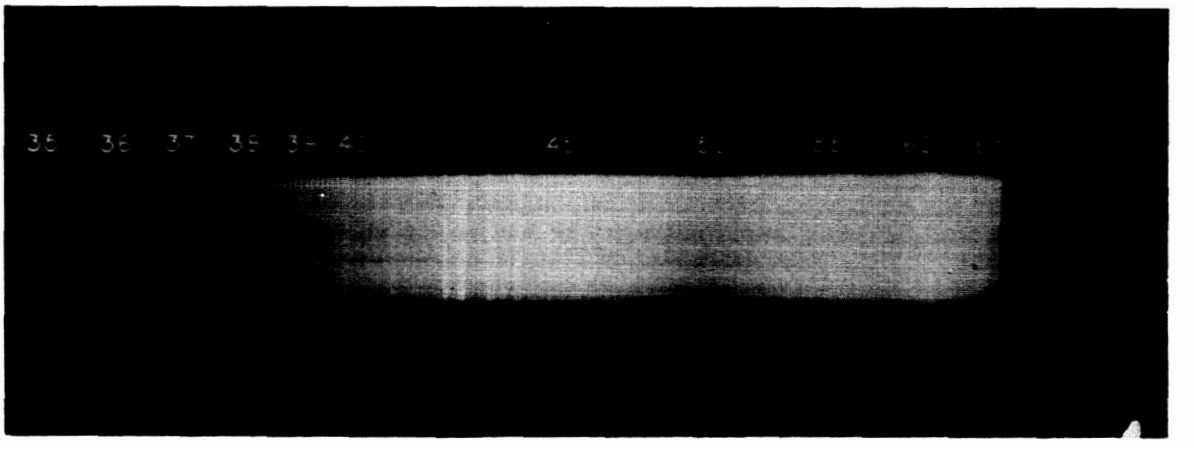

FIGURE 14 TIME INTEGRATED SPECTROGRAM
(Kodak F-1 Photographic Plates)

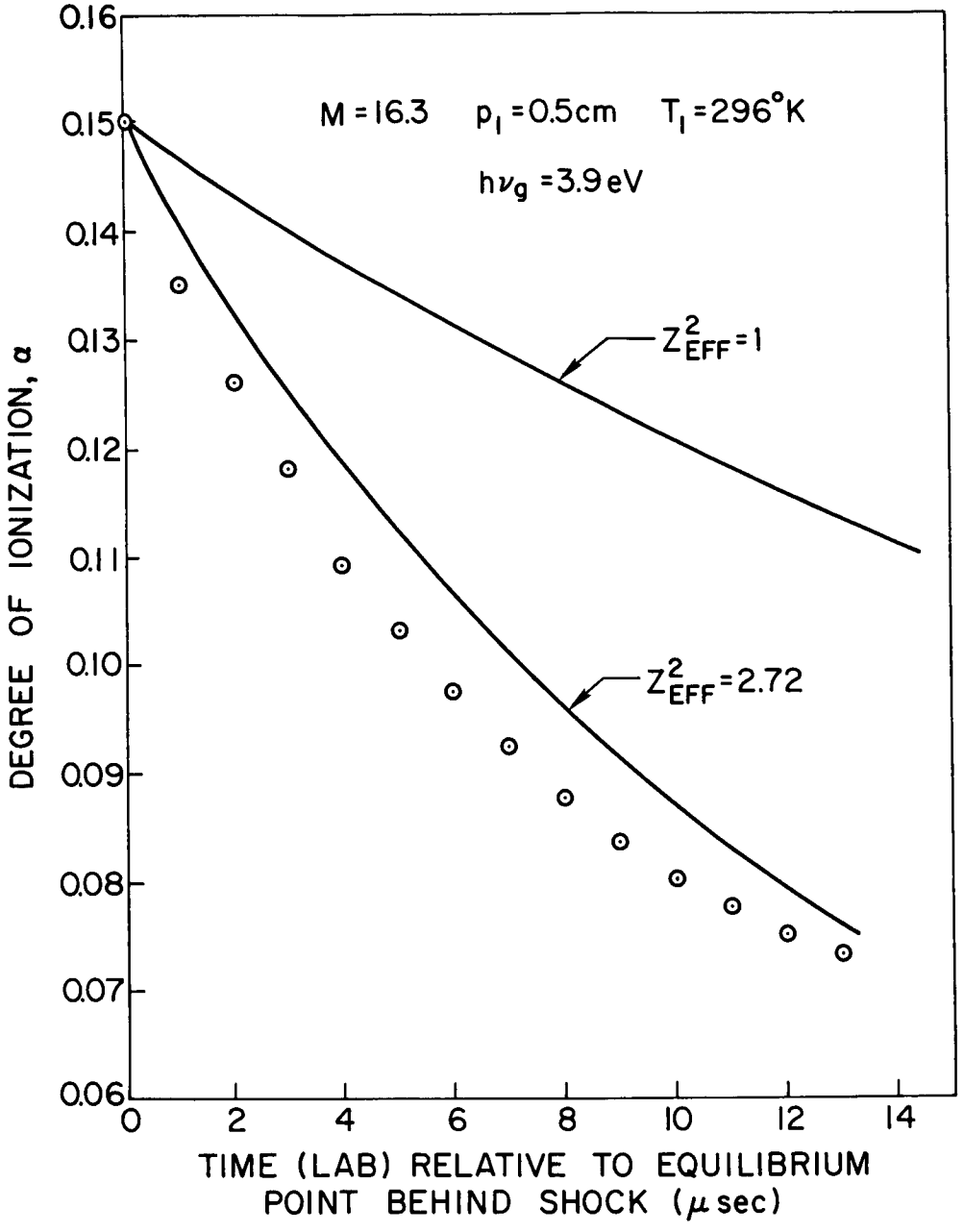

FIGURE 15 COMPARISON OF CONTINUUM THEORY WITH EXPERIMENTAL DATA OF DEGREE OF IONIZATION

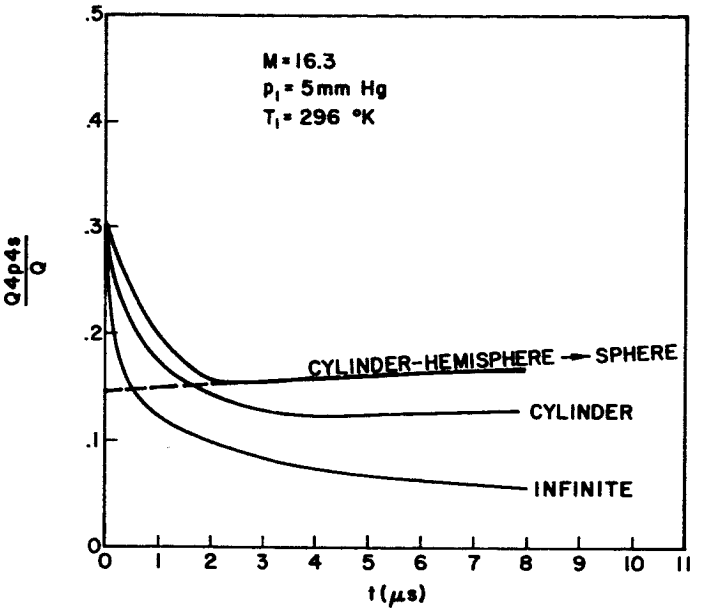

FIGURE 16 RADIATION ABSORPTION MODELS

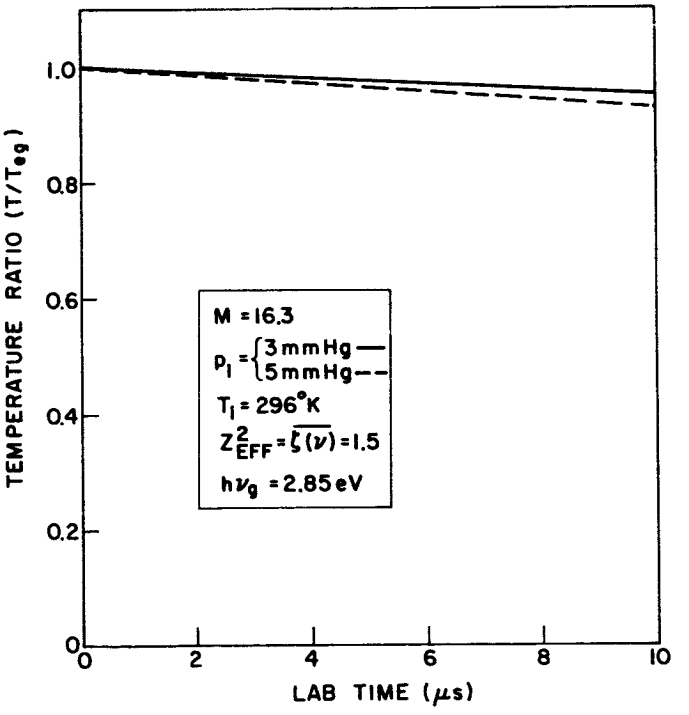

FIGURE 17 TEMPERATURE PROFILES

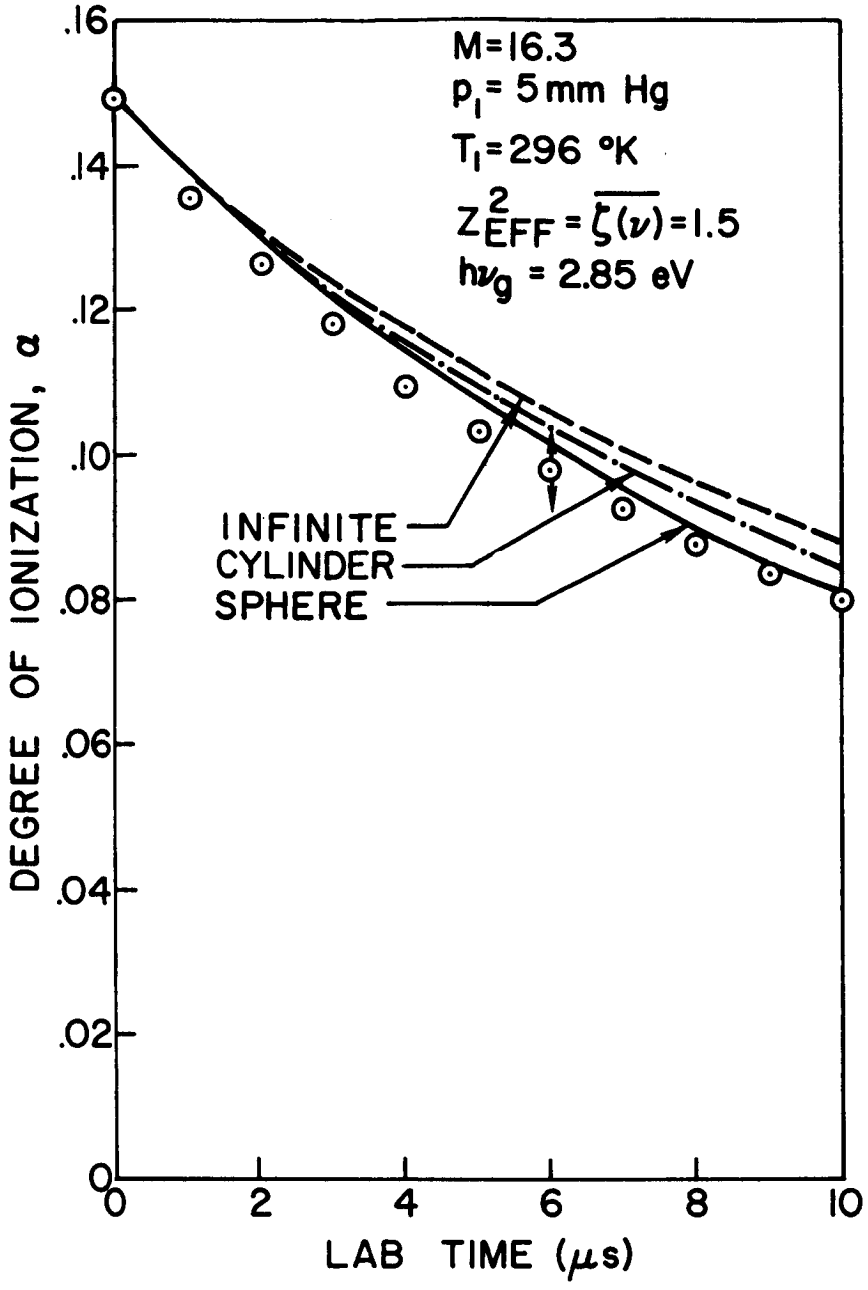

FIGURE 18 DEGREE OF IONIZATION PROFILE

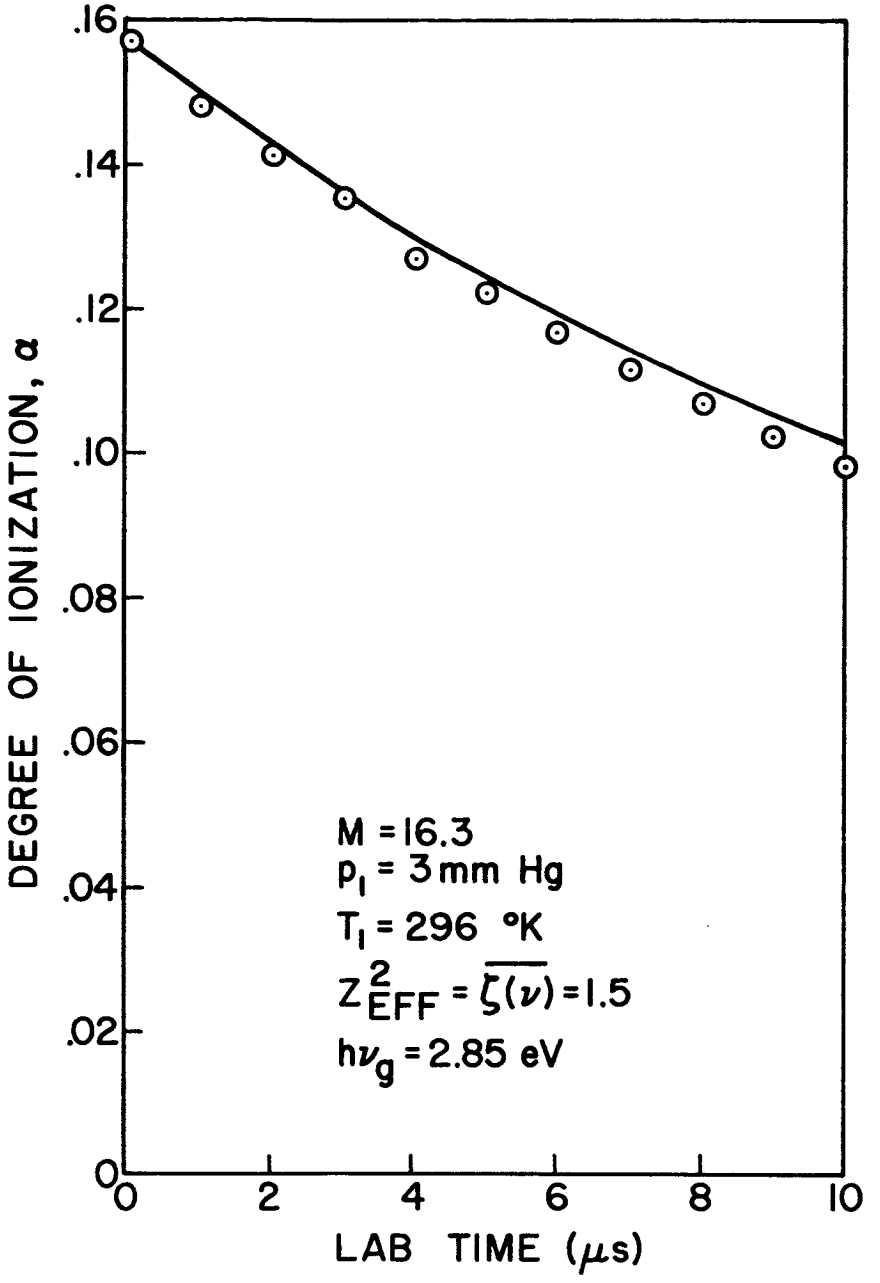

FIGURE 19 DEGREE OF IONIZATION PROFILE

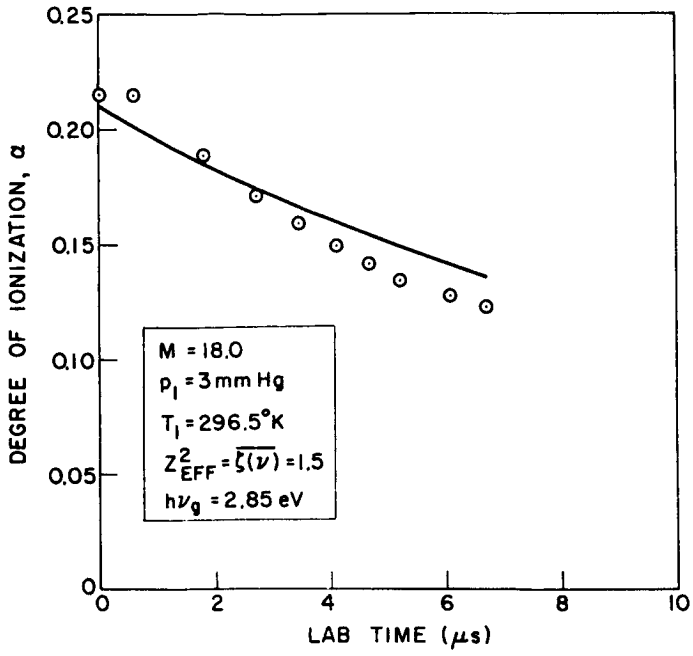

FIGURE 20 DEGREE OF IONIZATION PROFILE

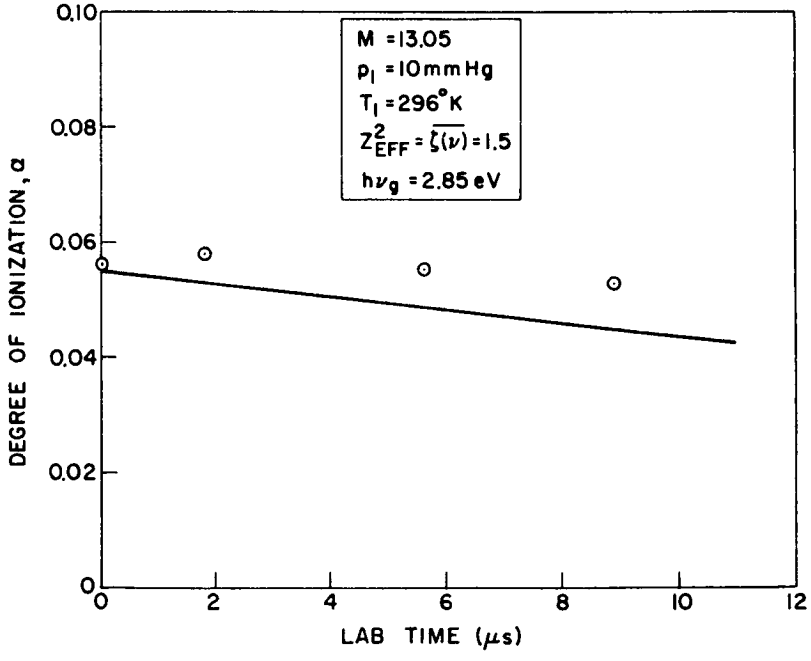

FIGURE 21 DEGREE OF IONIZATION PROFILE

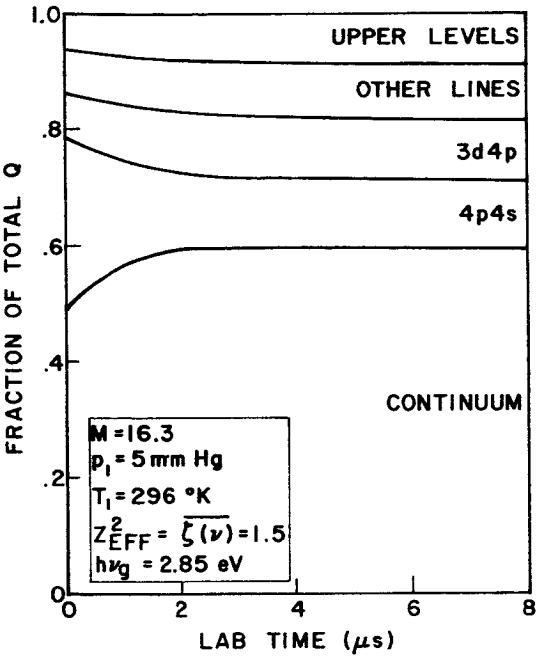

FIGURE 22 ENERGY LOSS PROFILE

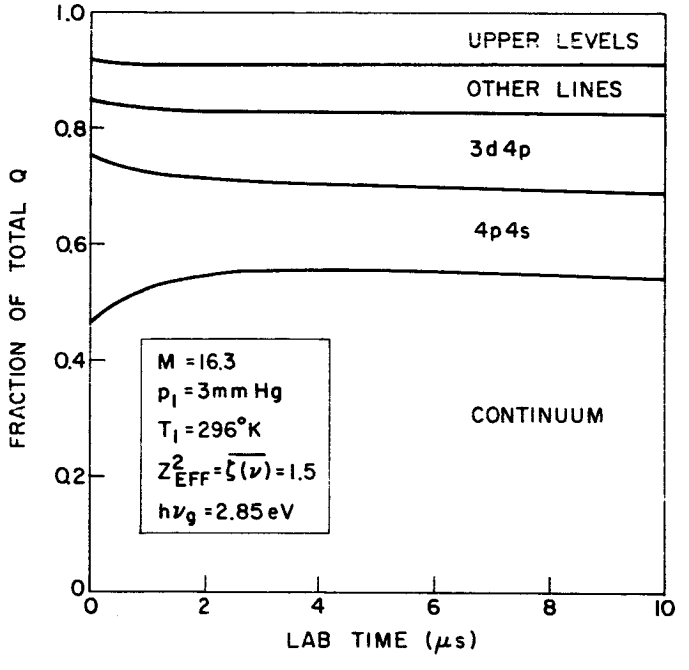

FIGURE 23 ENERGY LOSS PROFILE

5. SUMMARY AND CONCLUSIONS

Radiation losses associated with the flow behind strong normal shock waves in argon have been studied experimentally using as a diagnostic tool an optical Mach-Zehnder interferometer. By measuring the shift in fringes resulting from a change in the refractive index of the medium, a time history of both the electron and mass densities was recorded. The evidenced decreasing electron density indicated an energy loss mechanism occurring in the flow region outside of the electronic relaxation zone behind the incident shock wave. The experimental study was supplemented by a detailed analysis on the possible loss mechanisms. Theory and experiment were in good agreement.

The analysis indicated that the predominate single loss mechanism was continuum emission resulting from radiative recombination and Bremsstrahlung radiation. However line radiation losses were not negligible. Sizeable loss resulted from bound-bound transitions in argon between the lower excited levels, specifically the $4p4s$ and $3d4p$ transitions even though under test conditions these lines experienced absorption. Various absorption models were considered in order to estimate the energy loss by such transitions. Equally important was the accumulated energy loss resulting from highly excited level bound-bound transitions in argon. Bound-bound line radiation from the argon ion was not found to contribute significantly to the total energy loss. A consistent and realistic set of continuum theory parameters resulted when the theoretical analysis was correlated with the experimental data.

The values for these parameters agreed with the estimated quantum mechanical results of Biberman and Norman (9) and of Schlüter (10).

Loss of energy by radiative processes led to an appreciable reduction in the gas enthalpy. In order to perform a meaningful interferometric study on a partially ionized expansion flow a uniform upstream electron density of the order of 10^{17} cm^{-3} was required. Severe radiation losses encountered behind such strong shocks resulted in non-steady upstream flow. Under such conditions a parallel analytical investigation was unfeasible. This problem is discussed in Appendix 4.

APPENDIX 1

RADIATION ABSORPTION MODELS

Consider a finite volume of radiating gas of constant density and temperature. Introduce x as the distance measured from the shock front in shock coordinates, θ as the direction angle (colatitude) an intensity ray makes with the x axis, and φ as the azimuthal angle. For the case of axial symmetry,

$$d\Omega = \sin\theta \, d\theta \, d\varphi \, .$$

This condition exists along the center line of the shock tube. In general the rate of energy loss per unit volume is given by,

$$Q = Q^{+} + Q^{-}$$

$$= 2\pi \int_{0}^{\pi/2} \int_{\nu} k'_{\nu} B_{\nu} e^{-k'_{\nu} R(\theta)} \sin\theta \, d\theta \, d\nu$$

$$+ 2\pi \int_{\pi/2}^{\pi} \int_{\nu} k'_{\nu} B_{\nu} e^{-k'_{\nu} R(\beta)} \sin\beta \, d\beta \, d\nu \, .$$

Assume the isolated line can be represented by a dispersion type profile,

$$k'_{\nu} = \frac{A^{*} B}{(\nu - \nu_{o})^{2} + B^{2}}$$

where,

$$A^* = \frac{e^2 Nf}{m_e c}\left(1 - e^{-h\nu_o/kT}\right)$$

$$B = \frac{\Gamma}{4\pi} \quad .$$

Under these assumptions closed form solutions for Q can be obtained for several geometric gas domains.

1. Spherical volume model (R = constant)

In this case R corresponds to the effective radius of the cross section of the shock tube. Since R is independent of direction angle for this case,

$$Q = 4\pi \int_{\nu} k'_{\nu} B_{\nu} e^{-k'_{\nu} R} \, d\nu$$

$$= 4\pi B_{\nu_o} \int_{-\infty}^{\infty} \frac{A^* B}{(\nu - \nu_o)^2 + B^2} \exp\left[-\frac{A^* BR}{(\nu - \nu_o)^2 + B^2}\right] d\nu.$$

Introducing, $(\nu - \nu_o) = B \tan u$,

$$Q = 4\pi^2 B_{\nu_o} A^* e^{-A^* R/2B} I_0(A^* R/2B)$$

$$= \frac{4\pi^2 e^2 Nf}{m_e c} B_{\nu_o} \left(1 - e^{-h\nu_o/kT}\right) e^{-\tau_{\nu_o}/2} I_0(\tau_{\nu_o}/2)$$

where,

$$\tau_{\nu_o} = \frac{A^* R}{B} = \frac{4\pi e^2 Nf}{m_e c \Gamma}\left(1 - e^{-h\nu_o/kT}\right) R,$$

and $I_0(\tau_{\nu_o}/2)$ is the modified Bessel function of the first kind

of order zero. Values for this special function are tabulated in "Table of Functions" of Jahnke-Emde.

Two limiting cases based on optical depth exist:

i) Optically thin, $\tau_{\nu_o} \to 0$

$$Q(\nu_o) \to \frac{4\pi^2 e^2}{m_e c} B_{\nu_o} Nf(1 - e^{-h\nu_o/kT}) (1 - \tau_{\nu_o}/2) .$$

ii) Optically thick, $\tau_{\nu_o} \to \infty$

Here $e^{-\tau_{\nu_o}/2} I_0(\tau_{\nu_o}/2) \to (\pi\tau_{\nu_o})^{-1/2}$

$$Q(\nu_o) \to \frac{4\pi^{3/2} e^2}{m_e c} B_{\nu_o} Nf (1 - e^{-h\nu_o/kT}) \frac{1}{\sqrt{\tau_{\nu_o}}} .$$

Figure 24 shows the dependence of $Q(\nu_o)$ on optical depth for the exact solution and the two limiting case solutions.

2. Finite circular cross section model

Since $R = R(\theta)$, Q^+ and Q^- must be calculated separately. For Q^+,

$$R = x \sec\theta \qquad \text{for } 0 \le \theta \le \theta_{cr}$$

$$= \frac{L}{2} \csc\theta \qquad \theta_{cr} \le \theta \le \pi/2$$

$$\theta_{cr} = \tan^{-1}\left(\frac{L}{2}\right)$$

$\frac{L}{2}$ = radius of shock tube

then,

$$Q^{+} = 2\pi \int_{\nu} \left(\int_{0}^{\theta_{cr}} \sin\theta \; e^{-k'_{\nu} x \sec\theta} \, d\theta + \int_{\theta_{cr}}^{\pi/2} \sin\theta \; e^{-\frac{L}{2} k'_{\nu} \csc\theta} \, d\theta \right) B_{\nu} k'_{\nu} \, d\nu$$

$$= 2\pi \int_{\nu} (M + N) \, B_{\nu} k'_{\nu} \, d\nu \, .$$

Letting $z = \sec\theta$ yields

$$M = \int_{1}^{\infty} \frac{1}{z^2} e^{-k'_{\nu} x z} \, dz - \int_{z_{cr}}^{\infty} \frac{1}{z^2} e^{-k'_{\nu} x z} \, dz$$

$$= E_2(k'_{\nu} x) - \frac{x}{\sqrt{(L/2)^2 + x^2}} E_2\left(k'_{\nu} \sqrt{(L/2)^2 + x^2}\right)$$

$$= E_2(k'_{\nu} x) - (x/R_{cr}) \, E_2(k'_{\nu} R_{cr})$$

where,

$$R_{cr} = \sqrt{(L/2)^2 + x^2}$$

$E_2(c) \triangleq$ exponential integral of order two

$$\triangleq \int_{1}^{\infty} \frac{1}{z^2} e^{-cz} \, dz \, .$$

Also letting $u = \csc\theta$ yields,

$$N = \int_{1}^{\infty} \frac{du}{u^2\sqrt{u^2 - 1}} e^{-k'_{\nu} \frac{L}{2}} - \int_{u_{cr}}^{\infty} \frac{du}{u^2\sqrt{u^2 - 1}} e^{-k'_{\nu} \frac{L}{2}}$$

$$= F\left(\frac{L}{2} k'_{\nu}\right) - \frac{L/2}{R_{cr}} F(k'_{\nu} R_{cr})$$

where,

$$F(c) \triangleq \int_1^\infty \frac{du}{u^2\sqrt{u^2 - 1}} \; e^{-cu} \; .$$

Finally the expression for Q^+ reduces to,

$$Q^+ = 2\pi \, B_{\nu_o} \int_0^\infty \left[E_2(k'_\nu x) - \frac{x}{R_{cr}} E_2(k'_\nu R_{cr}) + F(\tfrac{L}{2} k'_\nu) - \frac{L/2}{R_{cr}} F(k'_\nu R_{cr}) \right] k'_\nu \, d\nu \; .$$

A similar approach can be used to evaluate Q^-. For the region of gas,

$$R'_{cr} = \sqrt{(L/2)^2 + x'^2}$$

$$x' = h - x$$

h = distance from ionization front to cold front.

Then,

$$Q = Q^+ + Q^- = 2\pi \, B_{\nu_o} \int_0^\infty \left[E_2(k'_\nu x) + E_2(k'_\nu x') - \frac{x}{R_{cr}} E_2(k'_\nu R_{cr}) \right.$$

$$- \frac{x'}{R'_{cr}} E_2(k'_\nu R'_{cr}) + 2F(\tfrac{L}{2} k'_\nu)$$

$$\left. - \frac{L/2}{R_{cr}} F(k'_\nu R_{cr}) - \frac{L/2}{R'_{cr}} F(k'_\nu R_{cr}) \right] k'_\nu \, d\nu \; .$$

Using the so-called "exponential approximation" the exponential integral is replaced by a purely exponential function of the form,

$$E_2(c) = a \, e^{-bc}$$

where the constants are a matter of choice. Two such sets of values are, (11)

$$(a,b) = \left(\frac{3}{4}, \frac{3}{2}\right)$$

$$= \left(1, 3^{\frac{1}{2}}\right)$$

For small c,

$$F(c) = 1 - c\,\frac{\pi}{2}$$

while for large u, F reduces to the form of the E_3 integral. It seems reasonable that F(c) can likewise be approximated by a simple exponential of the form,

$$F(c) = f\, e^{-gc}$$

where $(f,g) = (1, 5/4)$.

Using these exponential expressions Q can be integrated to yield,

$$Q(\nu_o) = \frac{2\pi^2 e^2 Nf}{m_e c} B_{\nu_o} \left[a e^{-Kbx} I_0(Kbx) + a e^{-Kbx'} I_0(Kbx') \right.$$

$$- \frac{ax}{R_{cr}} e^{-KbR_{cr}} I_0(KbR_{cr}) - \frac{ax'}{R'_{cr}} e^{-KbR'_{cr}} I_0(KbR'_{cr})$$

$$+ 2f\, e^{-Kg\,\frac{L}{2}} I_0\left(Kg\,\frac{L}{2}\right) - \frac{f(L/2)}{R_{cr}} e^{-KgR_{cr}} I_0(KgR_{cr})$$

$$\left. - \frac{f(L/2)}{R'_{cr}} e^{-KgR'_{cr}} I_0(KgR'_{cr}) \right] \left(1 - e^{-h\nu_o/kT}\right)$$

where,

$$K = \frac{A^*}{2B} = \frac{2\pi e^2 Nf}{m_e c\, \Gamma} \left(1 - e^{-h\nu_o/kT}\right) .$$

3. Infinite domain model

This case is a special case of the finite circular cross section model where $L/2x \to \infty$. The previous expression reduces to,

$$Q(\nu_o) = \frac{2\pi^2 e^2 Nf}{m_e c} B_{\nu_o} a[e^{-Kbx} I_0(Kbx) + e^{-Kbx'} I_0(Kbx')](1 - e^{-h\nu_o/kT})$$

where,

$$K = \frac{A^*}{2B} = \frac{2\pi e^2 Nf}{m_e c \Gamma} (1 - e^{-h\nu_o/kT}) .$$

Comparison of absorption models under typical conditions:

$R = L/2 = 2.5$ cm

$x = 2.5$ cm (fixed)

$h/L = 20$

$\tau_{\nu_o} = k'R$

$Q/4\pi^2 B_{\nu_o} A^*$	$\tau_{\nu_o} = 1$	$\tau_{\nu_o} = 10$
(thin)	1.0	1.0
sphere	0.646	0.182
cylinder	0.514	0.139
infinite	0.299	0.084

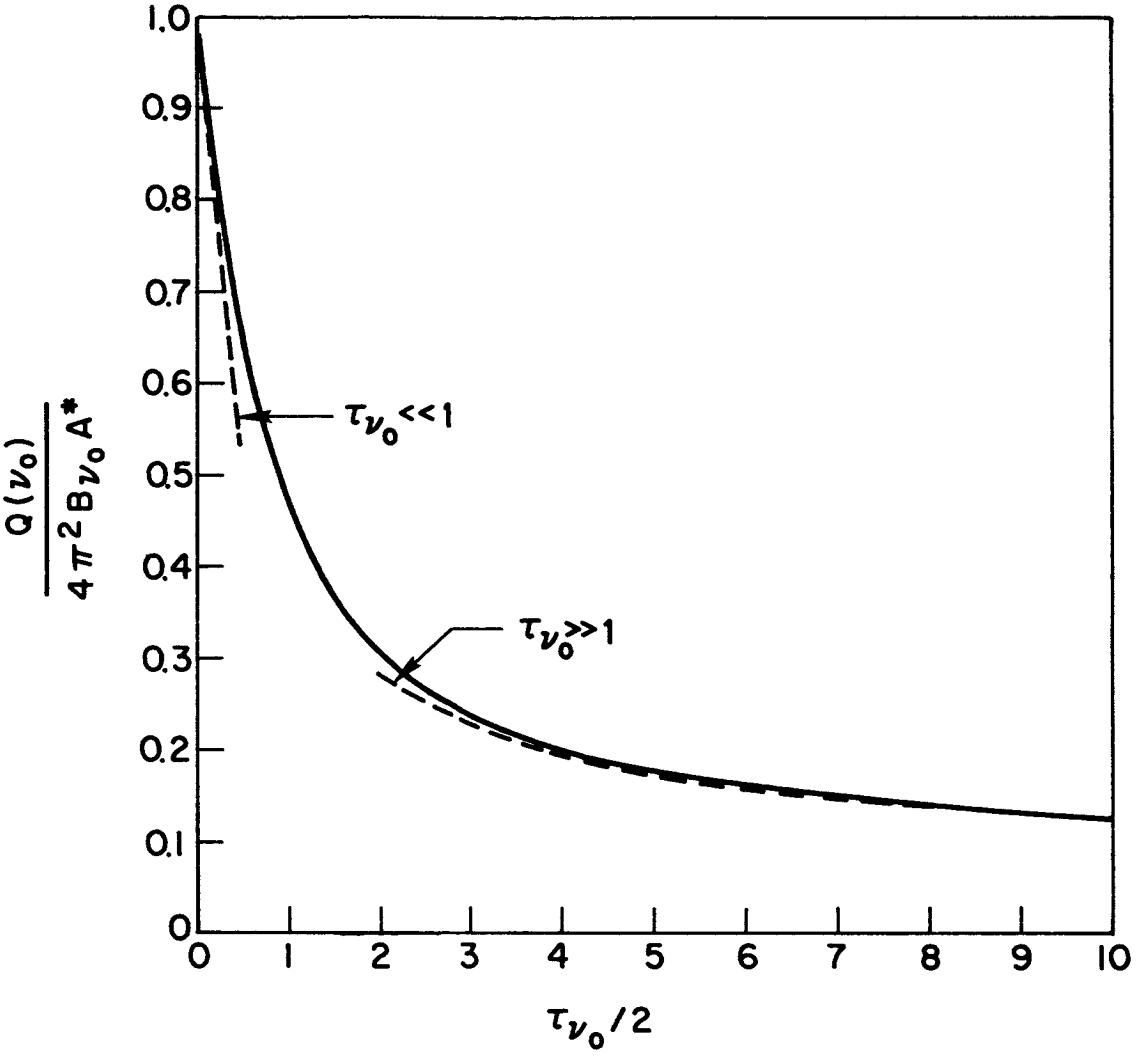

FIGURE 24 NORMALIZED RADIATION LOSS FOR SPHERICAL MODEL AS A FUNCTION OF OPTICAL DEPTH

APPENDIX 2

ARGON I ENERGY LEVELS

Argon is unfortunately an example of a complex spectrum (in place of series of singlet, doublet, and triplet energy levels there are multiple levels composed of four, five, ... regularly spaced levels). For argon the multiplicities of the levels are all odd--singlets, triplets, quintets, and septets.

Most complex spectra studied follow the Landé interval rule and thus reveal LS-coupling. Argon however along with the other rare gases reveal fairly good Jj-coupling (37). By Jj-coupling we assume there is considerable interaction between each ℓ_i and the s_i belonging to it, and not strong interaction of the ℓ_i with one another and the s_i with one another as in usual LS-coupling. Such coupling can be written symbolically as,

$$J = (j_1 \quad j_2 \quad j_3 \quad \ldots) \quad .$$

The core configuration for argon is $3p^5$, i.e., the ion of argon, while the normal $^1S_0$ state is given by the completed subshells of electrons only, the last of which is $3p^6$. For such a configuration of electrons the value of j for the core is,

$$J_c = \frac{1}{2} \, , \, \frac{3}{2} \quad .$$

Or, the ground state of the argon ion is,

$$^2P_{1/2},\ ^2P_{3/2}$$

Using Hund's rule the lowest is the $^2P_{3/2}$. (The degeneracy of the ground state of the ion is thus $4 + 2 = 6$.)

The Jj-coupling is then between the core (J_c) and the optical electron (j). One can build up the energy level diagram for argon (argon I) by simply placing the optical electron in the desired shell and observing the interaction with the core.

Example.

Consider the first excited state (one of the $3p^6$ electrons is raised to a $4s$ shell). The j of the $4s$ orbit is $\frac{1}{2}$ since $\ell = 0$. Then,

$$J = J_c + j, \ \ldots\ , \ |J_c - j|$$

So,

$$^2P_{1/2} : J = (\tfrac{1}{2} + \tfrac{1}{2}) \text{ and } (\tfrac{1}{2} - \tfrac{1}{2}) = 0 \text{ or } 1$$

$$^2P_{3/2} : J = (\tfrac{3}{2} + \tfrac{1}{2}) \text{ and } (\tfrac{3}{2} - \tfrac{1}{2}) = 1 \text{ or } 2$$

Therefore there are four levels of the $3p^5 4s$,

$$3p^5(^2P_{1/2})4s(J=1)$$

$$3p^5(^2P_{1/2})4s(J=0)$$

$$3p^5(^2P_{3/2})4s(J=1)$$

$$3p^5(^2P_{3/2})4s(J=2)\ .$$

The old Paschen notation would have labeled these levels as $1s_2$, $1s_3$, $1s_4$, $1s_5$.

In a similar manner it can be shown that there are 10 levels for the second excited state $(3p^5 4p)$ and 12 levels for the third excited state $(3p^5 3d)$.

As in LS-coupling certain selection rules must be obeyed for Jj-coupling. These are

$$\Delta j = 0, \pm 1 \quad (0 \text{ to } 0 \text{ excluded})$$

$$\Delta j = 0, \pm 1$$

Figure 25 on the next page shows the energy levels of the lower states for argon I. (Drawn from Ref. 38.) Note that there are two possible transitions from the first excited state $(3p^5 4s)$ to the ground state $(3p^6)$ and thirty transitions from the second $(3p^5 4p)$ to the first excited state $(3p^5 4s)$. The selection rules allow only these transitions. In general there are 30 principal series of spectrum lines and 30 sharp series of lines.

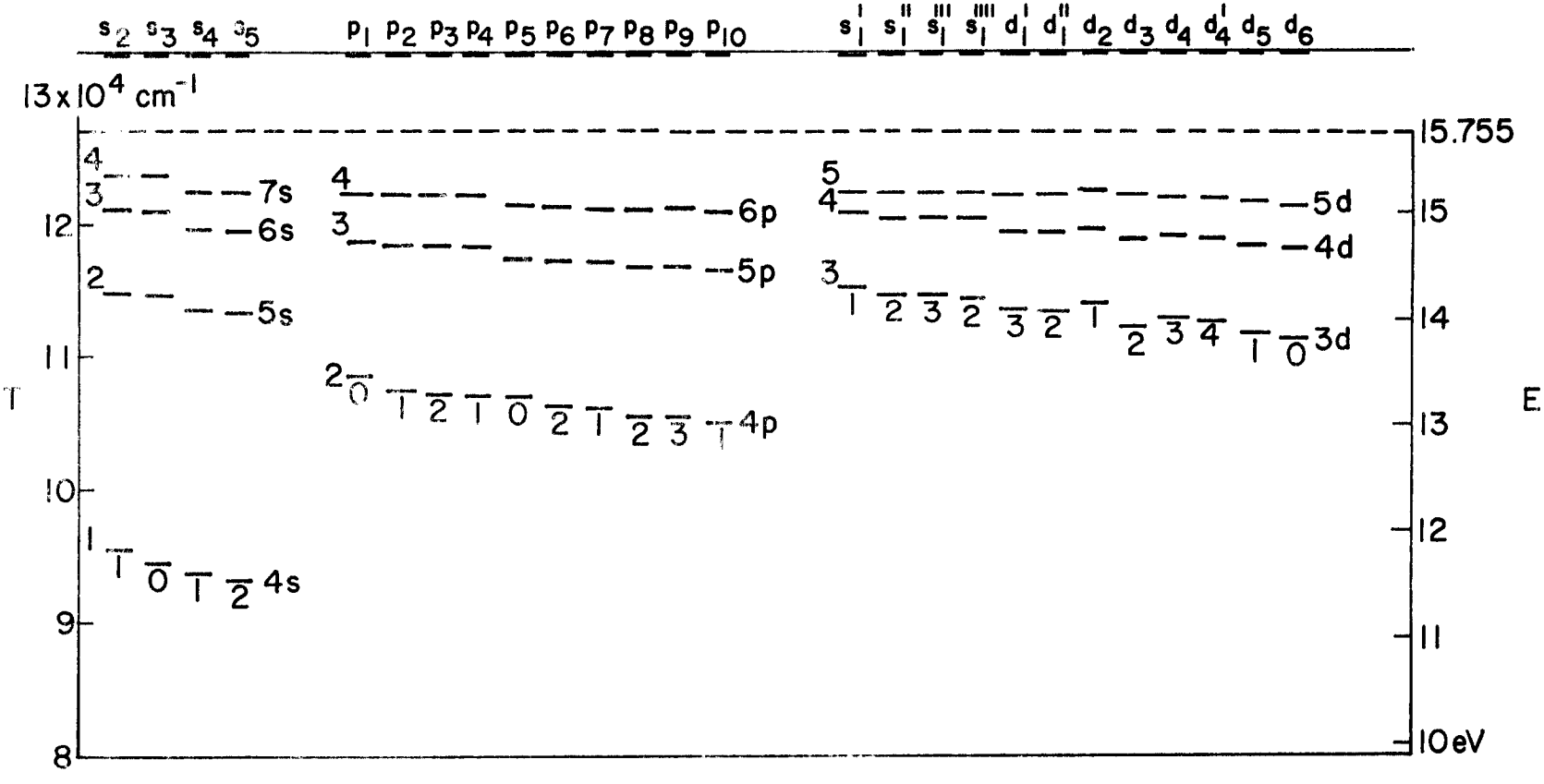

FIGURE 25 ARGON I ENERGY LEVEL DIAGRAM

APPENDIX 3

APPLICATION OF THE BATES AND DAMGAARD METHOD TO THE DETERMINATION OF ARGON I OSCILLATOR STRENGTHS

The oscillator strength f is related to the line strength S by,

$$f = S \frac{8\pi m_e c}{3he^2 g_L \lambda}$$

where λ is the wavelength of the radiation absorbed or emitted and g_L is the statistical weight of the lower level concerned in the transition. Now it can be shown (21) that

$$S = \zeta(m)\ \zeta(\ell)\ \sigma^2$$

where $\zeta(m)$ is a factor depending on the particular multiplet of the transition array, $\zeta(\ell)$ is a factor depending on the particular line of the multiplet, and σ^2 is defined by

$$\sigma^2 = \frac{1}{(4\ell_>^2 - 1)} \left(\int_0^\infty R_L\ r\ R_u\ dr\right)^2$$

$\ell_>$ being the greater of the two azimuthal quantum numbers involved in the transition.

Goldberg (39) states that in a transition array such as $n\ \ell^k\ n'\ \ell' - n\ \ell^k\ n''\ \ell''$ the sum of the absolute strengths of all

the multiplet originating from or ending in a term of $n\,\ell^k\,n'\,\ell'$ is equal to,

$$\sum \zeta(m)\ \zeta(\ell) = \begin{cases} g'_{\ell}(\ell' + 1)(2\ell' + 3) & \text{for } \ell'' = \ell' + 1 \\ g'_{\ell}(\ell')(2\ell' - 1) & \text{for } \ell'' = \ell' - 1 \end{cases}.$$

As noted by Rohrlich (40) when j-j coupling is important (as in argon I) comparison of theoretical expressions of particular lines of the multiplet with observed values is not in general possible. However for the sum of all the multiplet line of a given transition this technique should give useful values. For argon the degeneracy of the ℓ' level is related to that of hydrogen by

$$g'_{\ell} = \gamma\, g'_{H\ell}$$

where γ equals 6 for the argon atom. (The six is due to the ground state degeneracy of the argon ion.)

Hence the expression for the line strength S due to all the lines associated with a certain transition is,

$$S = \begin{cases} 12(2\ell' + 1)(\ell' + 1)(2\ell + 3) & \text{for } \ell'' = \ell' + 1 \\ 12(2\ell' + 1)(\ell')(2\ell' - 1) & \text{for } \ell'' = \ell' - 1 \end{cases}.$$

And the expression for the rate of energy lost per unit volume in terms of the line strength S for an optically thin transition becomes simply,

$$Q(\nu_{UL}) = \frac{4h^4}{3c^3 m_e^2 e^2}\ \nu_{UL}^4\ \frac{N_a}{g_0}\ e^{-E_{ou}/kT}\ S\ .$$

The Bates and Damgaard method is based on the fact that in calculating the transition integrals $(\int_0^\infty R_L\, r\, R_U\, dr)^2$ it is permissible to neglect the departure of the potential of an atom from its asymptotic Coulomb form. This enables one to derive a general analytical expression for the transition integral.

In the standard central field model the radial wave functions R_L and R_U satisfy the differential equation,

$$\frac{d^2R}{dr^2} + \left(2V - \frac{\ell(\ell+1)}{r^2} - \epsilon\right) R = 0$$

where V is the potential and ϵ is the energy eigenvalue. The potential V is replaced by its asymptotic Coulomb form C/r, where C is the excess charge on the nucleus when the optical electron is removed. In this technique the energy eigenvalues are forced to their correct values by introducing an effective principal quantum number which may be a non-integer.

APPENDIX 4

APPLICATION OF RADIATION LOSSES TO THE PROBLEM OF EXPANDING FLOW

Since the Prandtl-Meyer flow is one of the most important problems studied in non-reacting ideal gas flow, the investigation of the reacting, partially ionized flow problem seems equally essential in understanding high temperature gas dynamics. One is especially interested in the state of the gas as it passes through the expansion fan. Since the flow time of a particle increases with radial distance from the expansion corner, the flow passes from a frozen state near the corner to an equilibrium state very far from the corner. The partially ionized "Prandtl-Meyer" flow hopefully provides a means of producing steady state non-equilibrium flow suitable for laboratory experiments.

Extensive theoretical studies have been made of nonequilibrium expansion flow of ionizing monatomic gases around a corner. This problem is considerably more difficult than the classical Prandtl-Meyer flow, because of the nonlinear coupling between the chemical reaction and the flow variables. The limiting cases of thermal equilibrium and frozen flow are exceptions.

As in the classical Prandtl-Meyer flow of a non-reacting gas, no characteristic length is contained explicitly in the solution for equilibrium chemical reaction. This implies that the flow variables

are constant along any radial line drawn from the expansion corner. For a two-dimensional, steady, irrotational, inviscid, non-heat conducting, non-radiating ionized flow the following equations describe such a flow,

mass:
$$\rho u_r + \rho \frac{du_\theta}{d\theta} + u_\theta \frac{d\rho}{d\theta} = 0$$

momentum e_r direction:
$$\frac{u_\theta}{r}\left(u_\theta - \frac{du_r}{d\theta}\right) = 0$$

momentum e_θ direction:
$$u_r u_\theta + u_\theta \frac{du_\theta}{d\theta} + \frac{1}{\rho}\frac{dp}{d\theta} = 0$$

energy:
$$\frac{dh}{d\theta} - \frac{1}{\rho}\frac{dp}{d\theta} = 0$$

state:
$$p = \rho(1 + \alpha)\, RT$$

Saha:
$$\frac{\alpha^2}{1-\alpha^2} = \left(\frac{2\pi m_e}{h^2}\right)^{3/2} \frac{2z_i^{el}}{z_a^{el}} \frac{(kT)^{5/2}}{p} e^{-\beta/T}$$

All flow quantities depend only on the angle θ (see Fig. 26). Since the motion is irrotational and steady, entropy must be constant throughout the flow field for a flow of constant stagnation enthalpy. Introducing the equilibrium speed of sound for ionized flow, (41)

$$a_e^2 = \gamma^*(1 + \alpha)\, RT$$

$$\gamma^* = \frac{2}{(2-\alpha)(1+\alpha)} \frac{5(1+\alpha) + \alpha(1-\alpha^2)\left(\frac{5}{2} + \frac{\beta}{T}\right)^2}{3(1+\alpha) + \frac{2\alpha(1-\alpha)}{2-\alpha}\left(\frac{3}{2} + \frac{\beta}{T}\right)^2}$$

and using the fact of constant entropy, the problem can be solved numerically for the flow variables. Such a numerical solution program was written where the inputs are the upstream velocity, degree of ionization, equilibrium temperature, and pressure.

Figure 27 is a plot of expected fringe shift through an equilibrium expansion as a function of Mach number for an initial pressure of 3 mm Hg of argon, assuming the upstream flow (state 2) is at the thermal equilibrium state predicted from shock relations using the Saha equation. Notice that a fringe shift of the order of unity is expected for strong shocks. These fringe shifts are adequate enough to encourage interferometric investigation.

The other limiting case of flow with chemical reaction is "frozen" flow. In "frozen" flow the degree of ionization remains constant throughout the expansion. This problem is identical to the classical Prandtl–Meyer solution where the isentropic index is 5/3 for a monatomic gas.

For non-equilibrium flow the Saha equation is replaced by a rate equation. A knowledge of the mechanisms for ionization and recombination is now required. Most authors utilize the Petschek and Byron (33) ionization rate equation based on the assumption that the ionization rate is the same as the rate of excitation to the first excited state. Experimental studies of Wong (1) using optical interferometry essentially verify this ionization rate expression. Recombination is due to radiative recombination and three-body (and collisional deexcitation) recombination. Bray and Wilson (42) assume that radiative

recombination can be neglected with respect to three-body recombination for dense plasmas.

Three methods of attack have been used in attempting to solve this difficult problem--linearized solutions, power series expansions, and method of characteristics. The logical first step is to try solutions for special linearized cases since most difficulty stems from the nonlinear coupling. Clarke (43) used Laplace transforms while Ryhming (44) tried Green's functions. Napolitano's (45) method essentially consists of expanding all flow variables in terms of non-dimensional distance. Cleaver (46) and Appleton (47) utilized the method of characteristics for the solution of an ideal dissociating gas. Glass and Takano (41) solved the steady non-equilibrium expansion flow of ionized argon around a corner by the characteristics method. They used the previously mentioned rate equation assuming the atom and electron temperatures were identically equal. Kramer (48) assumed $T_e \neq T_A$ using the Petschek and Byron energy balance equation to relate the two temperatures. Wierum (49) was able to solve the problem approximately, assuming the pressure distribution along a streamline and the shape of a streamline in a non-equilibrium Prandtl-Meyer flow were identical to the equilibrium values with the same initial condition.

Unfortunately experimental efforts have not been so fruitful. Glass and Kawada (50) first investigated the feasibility of using optical interferometry to study a partially ionized Prandtl-Meyer flow. This problem was a logical extension of Wong's (1) work on the thermal equilibration of a shock heated plasma.

Initial "snap shot" interferograms were recorded of the flow expanding about a fifteen degree corner. Since the gas itself was radiating for such strong incident shocks, a Kerr Cell system (as explained in Chapter 3) was incorporated to limit the exposure time on the recording film. For such an expansion near equilibrium flow was anticipated. A typical interferogram utilizing vertical fringes is shown in Fig. 28. The resulting fringe shift through the expansion fan was less than the predicted value based on equilibrium (Saha) upstream conditions for both limiting cases of frozen and equilibrium flow. From these preliminary tests it was concluded that Saha conditions could not exist upstream. Thus extensive investigation of the radiation losses associated with the flow behind the incident shock was conducted (Chapters 2, 4).

Using the results of Chapter 4 theoretical predictions were made of the fringe shift through a fifteen degree expansion. The results were somewhat discouraging. Adequate fringe shift could only be expected for flow immediately behind the "ionization" front, where unfortunately the flow was nonsteady. Quasi-steady flow, reached after several microseconds after passage of the incident shock, resulted in insufficient fringe shift for interferometric studies. Therefore this phase of the research appeared at first to be disappointing. Several conclusions could however be drawn from such an experimental investigation.

The "snap shot" interferograms yielded useful information about the flow near the first Mach angle. The sensitivity in detecting gradients in electron density using interferometry was $\Delta\theta < 0.5$ degrees.

The angle of the first Mach line lead to a direct measurement of the upstream flow Mach number, M_2. Hence the local speed of sound was determined from a knowledge of the upstream flow velocity. The results are shown in Fig. 30 where upstream flow Mach number, M_2, is plotted as a function of incident shock Mach number, M_s. In all cases the experimental points lie on the local equilibrium speed of sound curve. The points even obeyed the transient curves, constructed from the radiation loss numerical solution of Chapter 2. Thus an independent check was made on the flow quantities behind the incident shock through this experimental measurement of the first Mach angle.

Since "snap shot" interferometric techniques proved unfeasible for studying the state of the ionized gas through the expansion, rotating mirror camera interferograms were attempted. Figure 29 shows a typical interferogram for $M = 18.0$, $p_1 = 3$ mm Hg, and $\lambda = 5890$ Å. (The slit was positioned as shown in Fig. 31.) Under such a configuration a time history of the fringe shift was recorded. The reduced interferograms yielded fringe shifts throughout the expansion. In Fig. 31 data points are shown for conditions corresponding to θ less than the first Mach angle and θ greater than the final Mach angle assuming equilibrium flow. In the former case good agreement was found when the data points were compared to the theoretical solution for flow behind the incident shock. In the latter case fair agreement was found when the data points were compared to the steady state equilibrium expansion solution using time dependent initial conditions determined from the radiation loss program. Thus the flow

appeared to remain in near equilibrium throughout the expansion under these test conditions. Other tests at different initial pressures and shock Mach numbers also indicated the same result.

In conclusion results from an optical interferometric study of a partially ionized expansion flow seem inconclusive, since adequate fringe shift can only be obtained under strong incident shocks in a flow region where the upstream flow is nonsteady. The extreme complexity of solving such a nonsteady, radiating, reacting expansion flow prevents in general parallel analytical study.

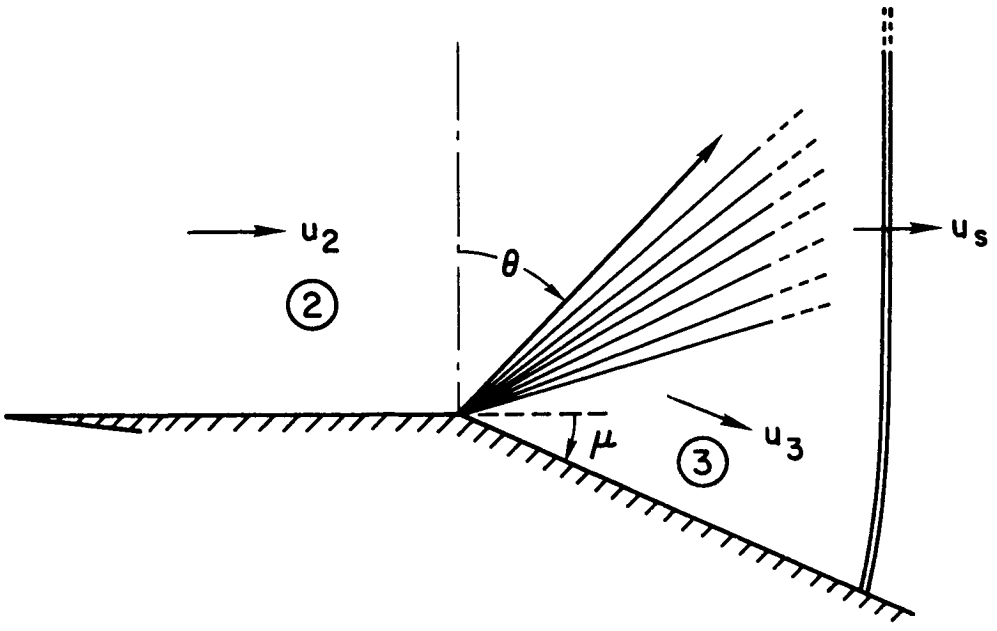

FIGURE 26 PRANDTL-MEYER EXPANSION

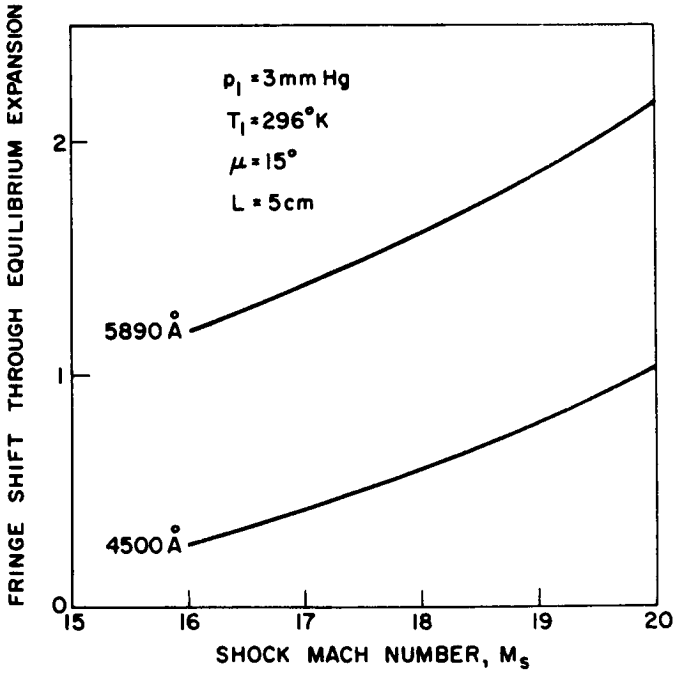

FIGURE 27 FRINGE SHIFT THROUGH EQUILIBRIUM EXPANSION RELATIVE TO EQUILIBRIUM CONDITIONS BEHIND THE INCIDENT SHOCK

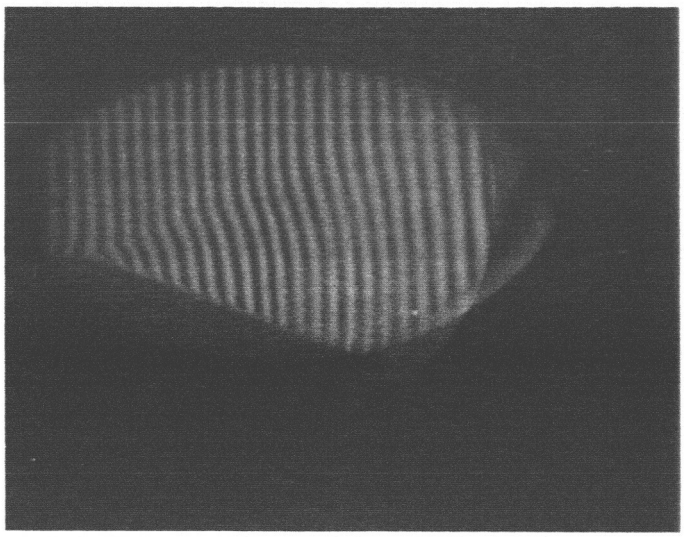

FIGURE 28 SNAP SHOT INTERFEROGRAM
($M = 18.6$, $p_1 = 3$ mm Hg)

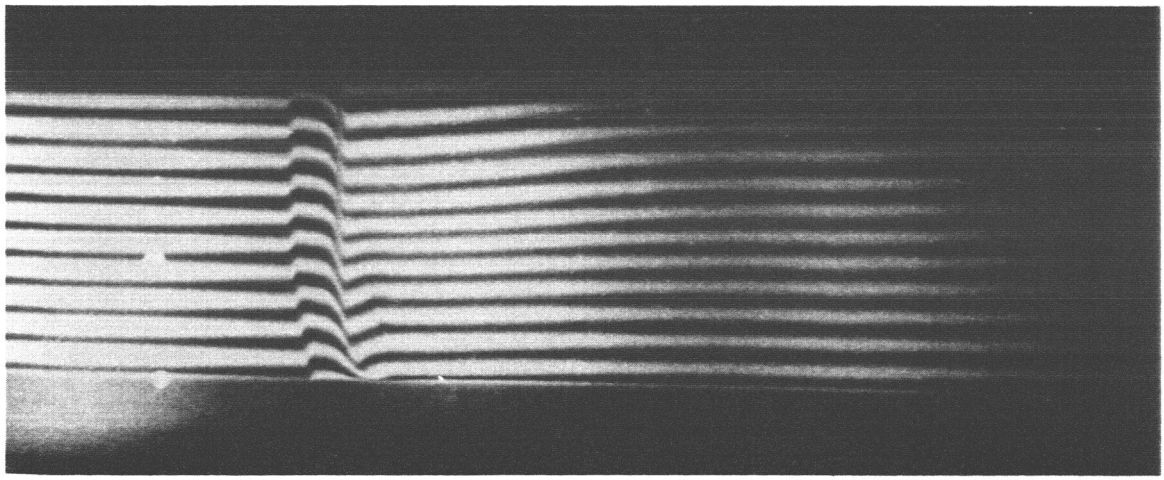

FIGURE 29 ROTATING MIRROR CAMERA INTERFEROGRAM
($M = 18.0$, $p_1 = 3$ mm Hg, $T_1 = 296°K$)

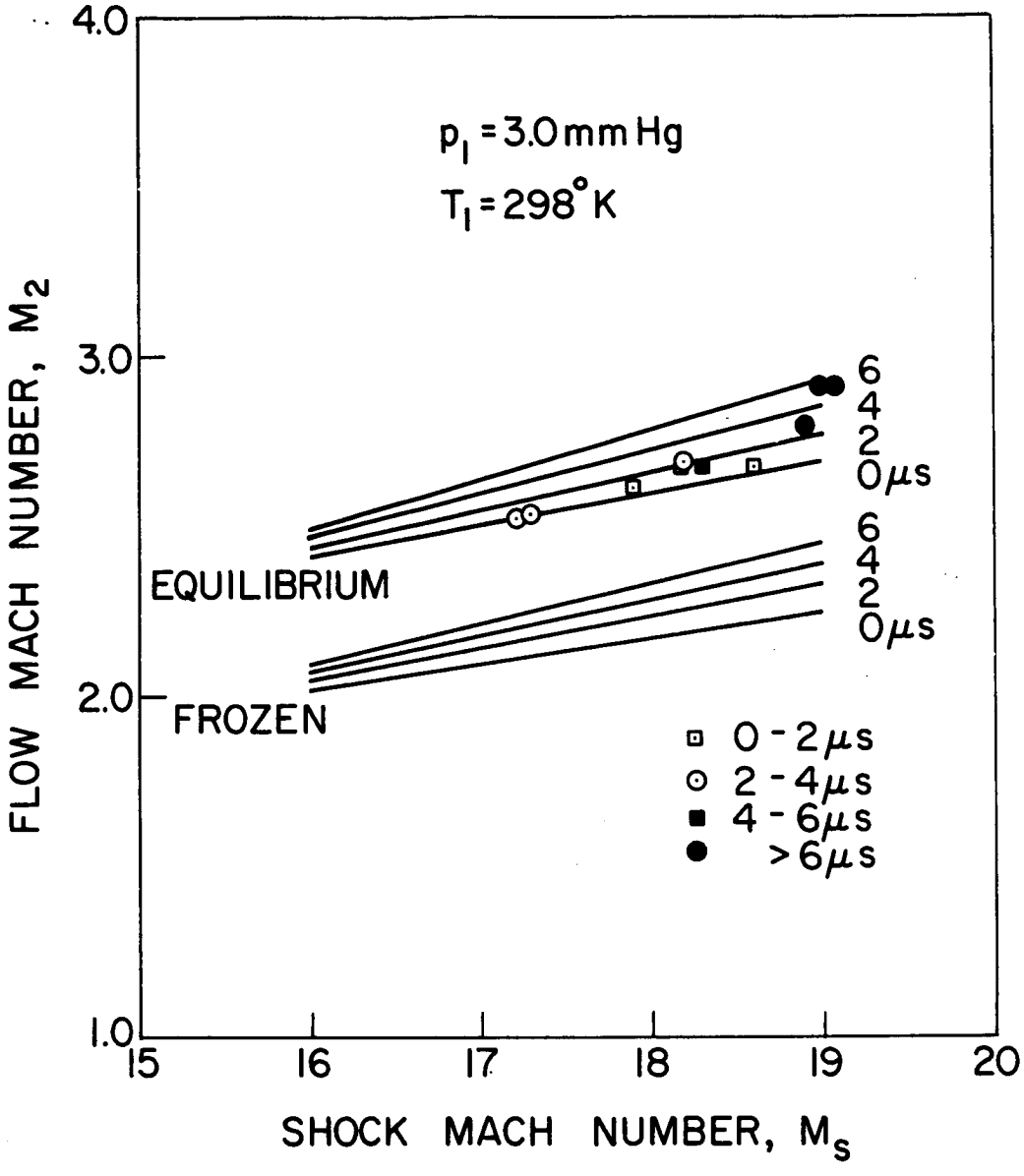

FIGURE 30 FLOW MACH NUMBER AS A FUNCTION OF SHOCK MACH NUMBER

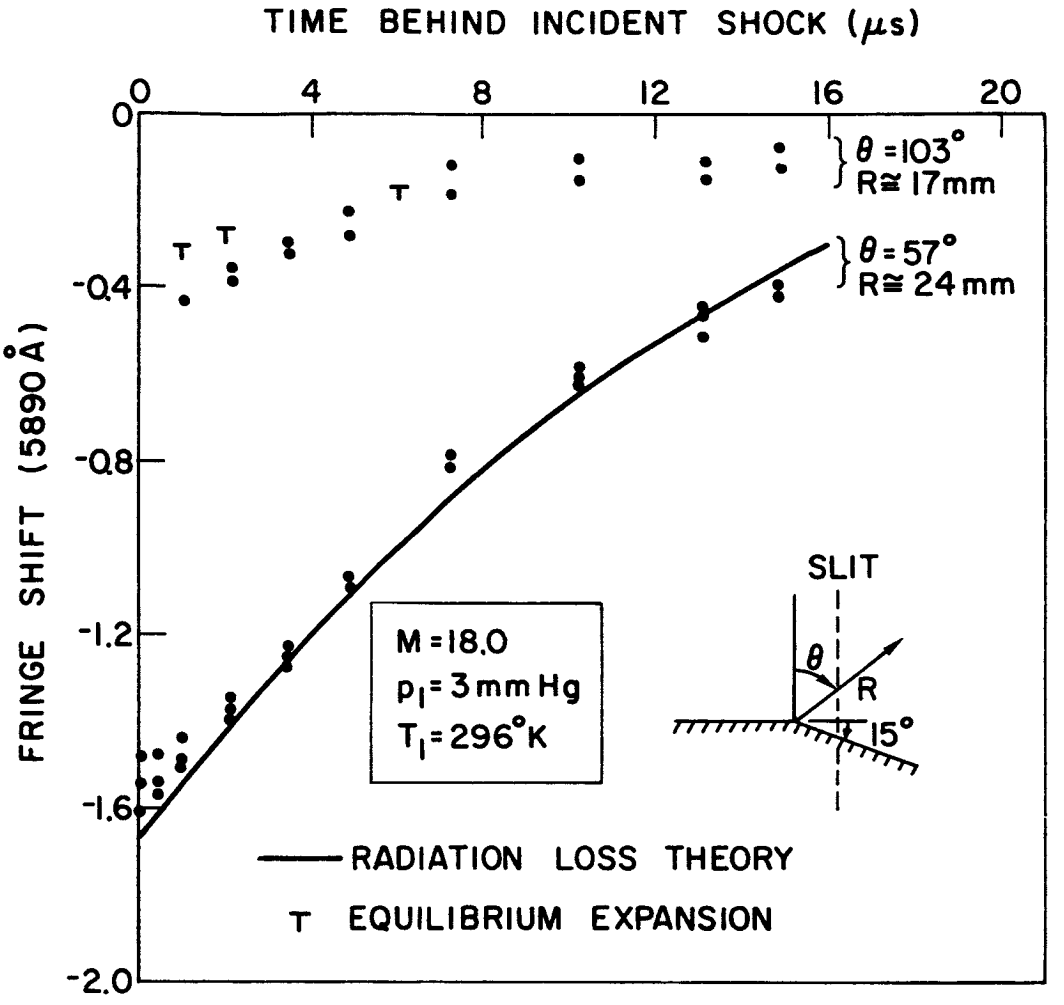

FIGURE 31 FRINGE SHIFT THROUGH EXPANSION AS A FUNCTION OF TIME BEHIND INCIDENT SHOCK

REFERENCES

1. Wong, H., Interferometric Study of Thermal Equilibration of a Shock Heated Plasma, Ph.D. Thesis, Stanford University, Stanford, California (1964).

2. Petschek, H.E., Rose, P.H., Glick, H.S., Kane, A. and Kantrowitz, A., J. Applied Physics 26, 83 (1955).

3. Pomerantz, J., J. Quant. Spectrc. Radiative Transfer 1, 185 (1961).

4. McChesney, M. and Al-Attar, Z., J. Quant. Spectrc. Radiative Transfer 5, 553 (1965).

5. Sevastyanenko, V.G., and Yakubov, I.T., Optics and Spectroscopy 16, 1 (1964).

6. Dronov, A.P., Sviridov, A.B., and Sobolev, N.N., Optics and Spectroscopy 12, 383 (1962).

7. Alpher, R.A. and White, D.R., Phys. of Fluids 7, 1239 (1964).

8. Rutowski, R.W. and Bershader, D., Phys. of Fluids 7, 568 (1964).

9. Biberman, L.M. and Norman, G.E., J. Quant. Spectrc. Radiative Transfer 3, 221 (1963); General Atomic translation, GA-tr-4943 (1963).

10. Schlüter, D., Astrophys. J. 61, 67 (1965).

11. Vincenti, W.G. and Kruger, C.H., Jr., Introduction to Gas Dynamics, John Wiley and Sons, New York (1965).

12. Zhigulev, V.N., Romishevskii, Ye. A., and Vertushkin, V.K., AIAA J. 1, 1473 (1963).

13. Bond, J.W., Jr., Watson, K.M. and Welch, J.A., Jr., Atomic Theory of Gas Dynamics, Addison-Wesley, Reading, Mass. (1965).

14. Sibulkin, M., NONR 562 35/7, Brown University, Providence, Rhode Island (1965).

15. Griem, H.R., Phys. Rev. 128, 997 (1962).

16. Griem, H.R., Plasma Spectroscopy, McGraw-Hill, New York (1964).

17. Gericke, W., Z. Astrophys. 53, 68 (1961).

18. Olsen, H.N., J. Quant. Spectrc. Radiative Transfer 3, 59 (1963).

19. Doherty, L.R., Ph.D. Thesis, University of Michigan, Ann Arbor, Michigan (1961).

20. Pery-Thorne, A., and Chamberlain, J.E., Proc. Phys. Soc. 82, 133 (1963).

21. Bates, D.R. and Damgaard, A., Phil. Trans. Roy. Soc. London 242, 101 (1949).

22. Knox, R.S., Phys. Rev. 110, 375 (1958).

23. Olsen, N.H., Phys. Rev. 125, 1703 (1961).

24. Biberman, L.M., Vorob'ev, V.S., and Norman, G.E., Optics and Spectroscopy 14, 176 (1963).

25. Aller, L.H., Astrophysics, Ronald Press (1953).

26. Karzas, W.J. and Latter, R., Astrophy. J. Suppl. VI, 55, 167 (1961).

27. Unsöld, A., Ann. Physik 33, 607 (1938).

28. Unsöld, A., Physik der Sternatmorpharen, 2nd ed., Springer-Verlag, Berlin (1955).

29. Vitense, E., Z. Astrophys. 28, 91 (1951).

30. Horst, D. Th. J. Ter. and Rutgers, G.A.W., Physica 19, 565 (1953).

31. Maecker, H. and Peters, T., Z. Phys. 139, 448 (1954).

32. Lagar'kov, A.N. and Yakubov, I.T., Optics and Spectroscopy 14, 103 (1963).

33. Petschek, H.E. and Byron, S.R., Ann. Physics 1, 270 (1957).

34. Tumakaev, G.K. and Lazovskaya, V.R., Soviet Physics-Technical Physics 9, 1449 (1965).

35. Alpher, R.A. and White, D.R., Phys. of Fluids 2, 153 (1959).

36. Slater, J.C., Phys. Rev. 36 (1930).

37. White, H.E., Introduction to Atomic Spectra, McGraw-Hill, New York (1934).

38. Moore, C.E., Atomic Energy Levels, vol. 1, NBS Circ. 467 (1949).

39. Goldberg, L., Astrophy. J. 84, 11 (1936).

40. Rohrlich, F., Astrophy. J., 441 (1959).

41. Glass, I.I. and Takano, A., UTIAS Rep. 95, University of Toronto, Toronto, Canada (1963).

42. Bray, K.N.C. and Wilson, J.A., U.S.A.A. Rep. 134, University of Southampton, Southampton, England (1960).

43. Clarke, J.F., College of Aeronautics Rep. 117, Cranfield, England (1958).

44. Ryhming, T.L., Jour. Aero/Astro Sci. 29 (1962).

45. Napolitano, L.G., AEDC-TN-50-129, Polytechnic Institute of Brooklyn, Brooklyn, New York (1960).

46. Cleaver, J.W., College of Aeronautics Rep. 123, Cranfield, England (1960).

47. Appleton, J.P., U.S.A.A. Rep. 146, University of Southampton, Southampton, England (1960).

48. Kramer, K., M.S. Thesis, Rice University, Houston, Texas (1964).

49. Wierum, F.A., Jr., Ph.D. Thesis, Rice University, Houston, Texas (1962).

50. Glass, I.I. and Kawada, H., UTIAS Rep. 85, University of Toronto, Toronto, Canada.